PHYSICAL REVIEW B **89**, 174105 (2014)

Influence of flexoelectric coupling on domain patterns in ferroelectrics

Rajeev Ahluwalia,[1] Alexander K. Tagantsev,[2,3] Petr Yudin,[2] Nava Setter,[2] Nathaniel Ng,[1] and David J. Srolovitz[4]

[1]*Institute of High Performance Computing, Singapore 138632*

[2]*Ceramic Laboratory, Swiss Federal Institute of Technology (EPFL), CH-1015 Lausanne, Switzerland*

[3]*Ferroics Laboratory, Ioffe Physical Technical Institute, St. Petersburg 194021, Russia*

[4]*Department of Materials Science and Engineering, Department of Mechanical Engineering, University of Pennsylvania, Philadelphia, Pennsylvania 19104, USA*

(Received 25 December 2013; revised manuscript received 14 April 2014; published 14 May 2014)

Using Ginzburg-Landau theory and two-dimensional (2D) phase field simulations, we analyze the influence of flexoelectric coupling on the domain patterns in ferroelectrics. The phase field simulations predict that a high strength of the flexoelectric coupling leads to formation of a fine structure in domain patterns in ferroelectrics. The fine structure forms when the coupling strength exceeds a critical value and is related to local transition into an incommensurate phase. Depending on the parameters, a structure with stripe patterns with antiparallel polarizations or another one, not seen before, with two-dimensional arrays of alternating vortices is found. Complex domain configurations with coexisting phases and unusual domain walls between them are observed. Although the incommensurate phase does not form for weaker couplings, the influence of flexoelectricity on bulk domain patterns can still be significant. The results of the calculations are rationalized using an analytical model. Directions for the modulation wave vectors in the fine structure are found in the framework of a linear analysis, while the type of the structure—stripes or vortices—is determined by anharmonicity.

DOI: 10.1103/PhysRevB.89.174105 PACS number(s): 77.80.Dj, 77.80.bn

I. INTRODUCTION

Ferroelectric transitions are usually accompanied by the formation of complex ferroelectric domain patterns that are associated with the coexistence of energetically equivalent polar variants [1]. The most important factors that govern the domain patterns are elastic interactions that arise from the electromechanical coupling and electrostatic interactions associated with bound charges. There is a growing body of evidence that a higher-order electromechanical coupling, known as flexoelectricity, can be important for ferroelectric materials, especially in domain walls [2,3]. Flexoelectricity is a coupling between electrical polarizations and strain gradients or, conversely, between strain and polarization gradients [4]. The presence of domain patterns in ferroelectrics necessarily implies the existence of strain and polarization gradients; this implies that flexoelectric effects could be playing an important role. In this paper we explore how this higher-order electromechanical coupling can influence the ferroelectric transition and the associated domain patterns.

Flexoelectric coupling in the bulk is characterized by flexocoupling constants f_{ijkl} that enter the electromechanical constitutive equations [4]

$$\begin{aligned} E_i &= \chi_{ij}^{-1} P_j - f_{klij} \frac{\partial \varepsilon_{kl}}{\partial x_j}, \\ \sigma_{ij} &= C_{ijkl} \varepsilon_{kl} + f_{ijkl} \frac{\partial P_k}{\partial x_l}, \end{aligned} \tag{1}$$

where the dummy suffix summation rule is accepted. Here E_i and σ_{ij} represent the electric and stress fields, ε_{ij} is the strain tensor, P_i is the polarization, C_{ijkl} is the elastic constant tensor, and χ_{ij}^{-1} are the components of the inverse dielectric susceptibility tensor. The flexocoupling coefficients f_{ijkl} are measured in volts and, according to estimates based on atomic considerations, are typically in the 1–10 V range [5].

Unlike piezoelectricity, which is observed only in noncentrosymmetric crystals, flexoelectricity is present in any materials [6,7]. This suggests a possibility of making piezoelectric devices from nanocomposites of nonpiezoelectric materials based upon flexoelectric properties [7,8]. Polarization switching induced by applying an external strain gradient such as bending or indentation has also been reported [9,10]. Recently a giant flexoelectric response associated with substrate-induced strain gradients has been observed in epitaxial $HoMnO_3$ films [11]. Recent work on $PbTiO_3$ thin films showed that substrate constraints can lead to an in-plane polarization component across *c* domains in an *a*/*c* domain pattern through flexoelectric coupling. This results in the rotation of the polarization inside *c* domains [12]. Recent theoretical work also shows the importance of flexoelectric effects in ferroelectric nanostructures [13]. These studies indicate that flexoelectric effects can strongly influence ferroelectric behavior.

The present research addresses the question of the nature of domain pattern formation in ferroelectrics in the presence of flexoelectric coupling. Besides being of fundamental interest, this is important for applications since it is well known (see, e.g., [14–16]) that domain patterns can strongly affect dielectric and piezoelectric properties. How does flexoelectric coupling influence the ferroelectric transition and the associated domain patterns? In general, flexoelectric coupling biases the system towards creating polarization and strain gradients. On the other hand, correlation interaction implies that creation of a gradient in polarizations costs extra energy. Thus we are dealing with competing interactions. Competing interactions can lead to formation of "incommensurate" or modulated structures in solids [17]. Already in 1970 [18], Axe *et al.* pointed out that the phonon dispersion curves

for the ferroelectric $KTaO_3$ suggest that mode coupling (which is, as presently known, due to flexoelectricity) can lead to the formation of the incommensurate state in perovskite ferroelectrics. In fact, a large number of ferroelectric materials are known to exhibit modulated phases [19–21]. Prior studies of incommensurate phases in ferroelectrics revealed the presence of one-dimensional modulations/stripe domain patterns. However, more complex modulations are also possible. For example, two-dimensional modulations have been observed in structural phase transitions in quartz where the appropriate order parameter is coupled to strain gradients [22]. Two-dimensional tweed modulations are also experimentally observed in ferroelastics as precursors to the martensite phase [23]. Do such complex modulated structures also exist in ferroelectrics? In the context of perovskite ferroelectrics with a cubic parent phase, there are three independent flexocoupling constants (f_{11}, f_{12}, and f_{44}). What kind of modulations arise from the couplings described by these constants? In this paper we perform simulations to observe the modulations associated with these three flexoelectric couplings, in context of a cubic to tetragonal ferroelectric transition.

We perform simulations within the Ginzburg-Landau framework, where the polarization components are the order parameters. For simplicity we restrict our analysis to a 2D model that describes domain patterns having continuous translational symmetry along the third dimension (z axis). In this approximation a ferroelectric undergoing a transition from a cubic to tetragonal phase can be viewed as a 2D ferroelectric undergoing a square to rectangular phase transition (see, e.g., [24]). The new feature of the present work is the incorporation of flexoelectric coupling in the Ginzburg-Landau framework (in addition to electrostrictive and electrostatic interactions, see, e.g., [24]). To understand the role played by each flexoelectric tensor component, we consider the cases: (i) $f_{44} \neq 0$, $f_{11} = f_{12} = 0$, (ii) $f_{11} \neq 0$, $f_{12} = f_{44} = 0$, and (iii) $f_{12} \neq 0$, $f_{11} = f_{44} = 0$, where f_{ij} are the flexocoupling coefficients (in Voigt notation) for a system undergoing a cubic to tetragonal transition.

Modulated patterns are expected to form when the flexoelectric coupling is sufficiently strong [18]. However, for relatively weak flexoelectric couplings, there will still be a tendency to create polarization and strain gradients. Thus, this coupling may influence domain patterns for bulk materials, even before the onset of the modulated phase. To what extent are the observed domain patterns in usual perovskite ferroelectrics influenced by the flexoelectric coupling? Even if the modulated patterns do not form, microstructural parameters, such as twin width, will be influenced by the flexoelectric coupling. To address these issues, we perform a parametric study of the influence of the flexoelectric coefficients on domain patterns. Since flexoelectricity is a coupling between polarizations and strain gradients, it is natural to expect that the domain patterns will be influenced by the mechanical boundary conditions. Thus we considered boundary conditions appropriate for both stress-free and mechanically constrained systems.

The paper is organized as follows. Section II provides an overview of the Ginzburg-Landau model with flexoelectric coupling. In Sec. III we present numerical simulation results for domain patterns for different flexoelectric couplings. An analytical treatment is presented in Sec. IV in order to help interpret the numerical results.

II. MODEL

We consider a two-dimensional (2D) model to describe domain patterns in a system with continuous translational symmetry along the third dimension (z axis). We assume that the component of the polarization along the translation axis is negligible ($P_z = 0$). In such cases, a perovskite ferroelectric undergoing a cubic to tetragonal phase transition can be viewed as an auxiliary 2D ferroelectric with a square to rectangular phase transition. The parameters for this 2D ferroelectric may be calculated from the properties of the three-dimensional (3D) ferroelectric (see, e.g., [24]).

The total free energy of the auxiliary 2D ferroelectric with flexoelectric coupling can be expressed as

$$F = \int d\vec{r}\,[f_{\text{Landau}} + f_{\text{elastic}} + f_{\text{flex}} + f_{\text{estat}}], \tag{2}$$

where $d\vec{r} = dxdy$. f_{Landau} is expressed in terms of the polarization $\vec{P}$ components[1] and their gradients as

$$\begin{aligned} f_{\text{Landau}} = {} & \alpha_1\left(P_x^2 + P_y^2\right) + \alpha_{11}\left(P_x^4 + P_y^4\right) + \alpha_{12}P_x^2P_y^2 \\ & + \alpha_{111}\left(P_x^6 + P_y^6\right) + \alpha_{112}\left(P_x^4P_y^2 + P_x^2P_y^4\right) \\ & + \sum_i \frac{\lambda_1}{2}\left[\left(\frac{\partial P_i}{\partial x}\right)^2 + \left(\frac{\partial P_i}{\partial y}\right)^2\right] \\ & + \sum_i \frac{\lambda_2}{2}\left[\left(\frac{\partial^2 P_i}{\partial x^2}\right) + \left(\frac{\partial^2 P_i}{\partial y^2}\right)\right]^2, \end{aligned} \tag{3}$$

where $i = x, y$. In this phenomenological model we describe the low-order gradient energy (quadratic in the first spatial derivatives of the polarization) choosing only one coefficient λ_1. For perovskite materials, in terms of the conventional fourth-rank tensor [26] g_{ijkl} for the correlation energy density with three independent coefficients g_{1111}, g_{1122}, and g_{1212}, such choice implies $g_{1111} = -g_{1122} = g_{1212} = \lambda_1$. These components satisfy the isotropic medium condition $g_{1111} - g_{1122} = 2g_{1212}$. Thus, the gradient energy used in our model corresponds to a specific type of isotropic medium. A higher-order gradient energy (quadratic in the second spatial derivatives of the polarization) is also described by only one coefficient λ_2. These simplifications are done in order to isolate the effect of flexoelectricity on the domain wall orientations from that of the anisotropy of the gradient energy. Note that the higher-order correlation energy is often omitted in the analysis of ferroelectric domain patterns. However,

[1]Strictly speaking, the Landau expansion for a ferroelectric should be written in terms of the ferroelectric contribution to the polarization [25] $\vec{P}_f = \vec{D} - \varepsilon_b\vec{E}$, where $\vec{D}$ is the electric displacement, $\vec{E}$ is the electric field, and ε_b is the background dielectric permittivity of the material. However, for the problems addressed here, the difference between $\vec{P}_f$ and $\vec{P}$ can be neglected.

it is important for the description of modulated structures [27].

The appropriate elastic energy, incorporating electrostrictive coupling, is

$$f_{\text{elastic}} = \frac{C_{11}}{2}\left[\left(u_{xx}-u_{xx}^0\right)^2+\left(u_{yy}-u_{yy}^0\right)^2\right] + C_{12}\left(u_{xx}-u_{xx}^0\right)\left(u_{yy}-u_{yy}^0\right)+\frac{C_{44}}{2}\left(u_{xy}-u_{xy}^0\right)^2, \tag{4}$$

where the linearized strain components are expressed in terms of the displacements u_i as $u_{xx} = (\partial u_x/\partial x)$, $u_{yy} = (\partial u_y/\partial y)$, and $u_{xy} \equiv (\partial u_x/\partial y + \partial u_y/\partial x)$. Here u_{ij}^0 represents the electrostrictive strain tensor:[2]

$$u_{xx}^0 = Q_{11}P_x^2 + Q_{12}P_y^2, \quad u_{yy}^0 = Q_{11}P_y^2 + Q_{12}P_x^2, \quad u_{xy}^0 = Q_{44}P_xP_y, \tag{5}$$

where Q_{ij} are the electrostrictive constants which couple strains and squares of polarizations. The contribution from the flexoelectric coupling can be expressed as

$$f_{\text{flex}} = -\frac{f_{11}}{2}\left(P_x\frac{\partial u_{xx}}{\partial x}+P_y\frac{\partial u_{yy}}{\partial y}-u_{xx}\frac{\partial P_x}{\partial x}-u_{yy}\frac{\partial P_y}{\partial y}\right) - \frac{f_{12}}{2}\left(P_x\frac{\partial u_{yy}}{\partial x}+P_y\frac{\partial u_{xx}}{\partial y}-u_{xx}\frac{\partial P_y}{\partial y}-u_{yy}\frac{\partial P_x}{\partial x}\right) - \frac{f_{44}}{2}\left[P_x\frac{\partial u_{xy}}{\partial y}+P_y\frac{\partial u_{xy}}{\partial x}-u_{xy}\left(\frac{\partial P_y}{\partial x}+\frac{\partial P_x}{\partial y}\right)\right]. \tag{6}$$

The total stresses, including the flexoelectricity contributions, are

$$\sigma_{xx} = \sigma_{xx}^e + \left[f_{11}\left(\frac{\partial P_x}{\partial x}\right)+f_{12}\left(\frac{\partial P_y}{\partial y}\right)\right],$$
$$\sigma_{yy} = \sigma_{yy}^e + \left[f_{11}\left(\frac{\partial P_y}{\partial y}\right)+f_{12}\left(\frac{\partial P_x}{\partial x}\right)\right], \tag{7}$$
$$\sigma_{xy} = \sigma_{xy}^e + f_{44}\left[\left(\frac{\partial P_y}{\partial x}\right)+\left(\frac{\partial P_x}{\partial y}\right)\right],$$

where σ_{ij}^e represents the electrostrictive part of the stress tensor

$$\sigma_{xx}^e = C_{11}\left(u_{xx}-u_{xx}^0\right)+C_{12}\left(u_{yy}-u_{yy}^0\right),$$
$$\sigma_{yy}^e = C_{11}\left(u_{yy}-u_{yy}^0\right)+C_{12}\left(u_{xx}-u_{xx}^0\right), \tag{8}$$
$$\sigma_{xy}^e = C_{44}\left(u_{xy}-u_{xy}^0\right).$$

The electrostatic contribution to the free energy is given as

$$f_{\text{estat}} = \left(\varepsilon_b\frac{\vec{E}\bullet\vec{E}}{2}\right), \tag{9}$$

where $\vec{E} = -\vec{\nabla}\varphi$ is the electric field, and φ and ε_b are the electrostatic potential and background dielectric permittivity of the material. The electrostatic potential can be calculated from Gauss's law $\vec{\nabla}\bullet\vec{D} = \rho(\vec{r})$, where $\vec{D} = \varepsilon_b\vec{E} + \vec{P}$ and ρ is the free charge density. Here we consider a system without free charge, for which Gauss's law leads to the following constraint:

$$\vec{\nabla}\bullet(-\varepsilon_b\vec{\nabla}\varphi+\vec{P}) = 0. \tag{10}$$

Polarization evolution kinetics are governed by the time-dependent Ginzburg-Landau equations

$$\frac{\partial P_i}{\partial t} = -\Gamma\left(\frac{\delta F}{\delta P_i}-E_i\right), \quad i = x,y, \tag{11}$$

where E_i is the electric field, Γ is a kinetic coefficient, and $\delta F/\delta P_i$ is the variational derivative of the free energy with respect to the polarization.

The full equations of motion can be expressed as

$$-\frac{1}{\Gamma}\frac{\partial P_x}{\partial t} = 2\alpha_1P_x+4\alpha_{11}P_x^3+2\alpha_{12}P_xP_y^2+6\alpha_{111}P_x^5+\alpha_{112}\left(4P_x^3P_y^2+2P_xP_y^4\right)-2P_x\left(Q_{11}\sigma_{xx}^e+Q_{12}\sigma_{yy}^e\right)-Q_{44}\sigma_{xy}^eP_y - f_{11}\left(\frac{\partial u_{xx}}{\partial x}\right)-f_{12}\left(\frac{\partial u_{yy}}{\partial x}\right)-f_{44}\left(\frac{\partial u_{xy}}{\partial y}\right)-\lambda_1\nabla^2P_x+\lambda_2\nabla^2(\nabla^2P_x)+\frac{\partial\varphi}{\partial x},$$
$$-\frac{1}{\Gamma}\frac{\partial P_y}{\partial t} = 2\alpha_1P_y+4\alpha_{11}P_y^3+2\alpha_{12}P_yP_x^2+6\alpha_{111}P_y^5+\alpha_{112}\left(4P_y^3P_x^2+2P_yP_x^4\right)-2P_y\left(Q_{11}\sigma_{yy}^e+Q_{12}\sigma_{xx}^e\right) - Q_{44}\sigma_{xy}^eP_x-f_{11}\left(\frac{\partial u_{yy}}{\partial y}\right)-f_{12}\left(\frac{\partial u_{xx}}{\partial y}\right)-f_{44}\left(\frac{\partial u_{xy}}{\partial x}\right)-\lambda_1\nabla^2P_y+\lambda_2\nabla^2(\nabla^2P_y)+\frac{\partial\varphi}{\partial y}, \tag{12}$$

where $\nabla^2 = (\partial^2/\partial x^2)+(\partial^2/\partial y^2)$ is the Laplacian operator. The displacement field dynamics are given by the dissipative force balance equations

$$\rho\frac{\partial^2u_x}{\partial t^2}-\eta\nabla^2\frac{\partial u_x}{\partial t} = \frac{\partial\sigma_{xx}}{\partial x}+\frac{\partial\sigma_{xy}}{\partial y},$$
$$\rho\frac{\partial^2u_y}{\partial t^2}-\eta\nabla^2\frac{\partial u_y}{\partial t} = \frac{\partial\sigma_{xy}}{\partial x}+\frac{\partial\sigma_{yy}}{\partial y}, \tag{13}$$

[2]There exist a confusion in the literature concerning the Voight notation for Q_{44}. Here we define $Q_{44} = 4Q_{2323}$.

TABLE I. Material parameters used in the simulations.

$\alpha_1 = -14.8\times10^7$ V m/C	$\alpha_{11} = -3.1\times10^7$ V m^5/C^3	$\alpha_{12} = 6.3\times10^8$ V m^5/C^3
$\alpha_{111} = 2.5\times10^8$ V m^9/C^5	$\alpha_{112} = 9.7\times10^8$ V m^9/C^5	$\lambda_1 = 1.5\times10^{-10}$ V m^3/C
$\lambda_2 = 5.9\times10^{-28}$ V m^5/C	$C_{11} = 1.7\times10^{11}$ N/m^2	$C_{12} = 7.9\times10^{10}$ N/m^2
$C_{44} = 1.1\times10^{11}$ N/m^2	$Q_{11} = 8.1\times10^{-2}$ m^4/C^2	$Q_{12} = -2.4\times10^{-2}$ m^4/C^2
$Q_{44} = 6.4\times10^{-2}$ m^4/C^2	$P_0 = 0.69$ C/m^2	

where η is a viscosity that is used to drive the system toward mechanical equilibrium $\partial\sigma_{ij}/\partial x_j = 0$. Equations (12) and (13) subject to the constraint (10) are used to study the dynamics of the polarizations.

III. SIMULATIONS OF BULK DOMAIN PATTERNS

To simulate the domain patterns, we solve Eqs. (10), (12), and (13) using a finite difference method. The computational domain is a square. To mimic a bulk system, we apply periodic boundary conditions for the polarizations and the electrostatic potential. For computational purposes, dimensionless length and time scales are introduced as $\vec{r}' = \vec{r}/\delta$ and $t^* = (t/\delta)\sqrt{C_{11}/\rho}$. The polarizations and displacements are scaled as $P_i = P_0 P_i^*$ and $u_i = Q_{11}P_0^2\delta u_i^*$, respectively. Here P_0 is a characteristic polarization and δ is the minimal spatial scale for our numerical simulations. The free energy parameteres are scaled as

$$\alpha_1^* = \alpha_1/|\alpha_1|, \quad \alpha_{11}^* = \alpha_{11}P_0^2/|\alpha_1|, \quad \alpha_{12}^* = \alpha_{12}P_0^2/|\alpha_1|,$$
$$\alpha_{111}^* = \alpha_{111}P_0^4/|\alpha_1|, \quad \alpha_{112}^* = \alpha_{112}P_0^4/|\alpha_1|.$$

The flexocoupling coefficients are scaled as $f_{ij}^* = (f_{ij}Q_{11}P_0/\delta|\alpha_1|)$. The rescaled gradient coefficients are expressed as $\lambda_1^* = \lambda_1/(\delta^2|\alpha_1|)$ and $\lambda_2^* = \lambda_2/(\delta^4|\alpha_1|)$. The rescaled viscosity and the kineatic coefficient are expressed as $\eta^* = \eta/\delta\sqrt{C_{11}\rho}$ and $\Gamma^* = \Gamma\,|\alpha_1|\,\delta\sqrt{\rho/C_{11}}$, respectively. The numerical simulations were performed using the dimensionless variables t^*, P^*, u^*, and r'.

We initialize the system with small, random fluctuations in the polarization around zero. Physically this corresponds to quenching from the paraelectric state into the ferroelectric one. The simulations are performed for the mechanically unconstrained $\langle\sigma_{xx}\rangle = \langle\sigma_{yy}\rangle = \langle\sigma_{xy}\rangle = 0$ as well as for the mechanically constrained $\langle u_{xx}\rangle = \langle u_{yy}\rangle = \langle u_{xy}\rangle = 0$ cases. Here symbol $\langle\rangle$ denotes averaging over the computational domain. We implement these mechanical conditions for a system with periodic boundary conditions using the method proposed by Khachaturyan and co-workers [28]. The details of our methodology are provided in Appendix A.

Although the results presented here can be applied to any ferroelectric, for our simulations we have used parameters close to those of Pb(Zr,Ti)O_3 (PZT) with a Ti content of 80% [29].

Since λ_1 and λ_2 are not known for PZT, we have chosen a value of λ_1 of the order of the coefficients for the gradient terms in $PbTiO_3$ and $BaTiO_3$ [1]. We choose λ_2 such that the terms controlled by λ_1 and λ_2 to be of the same order of magnitude when the polarization changes by its "atomic" value (e/a^2, where e and a are at a typical interatomic distance) at the distance a (as expected from order-of-magnitude estimates). Note that this set of the model parameters corresponds to a tetragonal homogeneous ferroelectric (i.e., the homogeneous ferroelectric state will correspond to a tetragonal system). In this context we speak of the "tetragonality" of the system.

Using the parameters from Table I we simulate bulk domain patterns for three different cases: $f_{11} = f_{44} = 0$, $f_{12} \neq 0$, $f_{12} = f_{44} = 0$, $f_{11} \neq 0$, and $f_{11} = f_{12} = 0$, $f_{44} \neq 0$. We first need to specify the kinetic parameters in Eqs. (12) and (13). In absence of reliable data for the viscosity and the mobility, we take $\Gamma^* = 1$ and $\eta^* = 10$. This choice of the kinetic coefficients ensures that mechanical equilibrium is established faster than polarization relaxation. For each case, we initiate the structure in a random paraelectric condition, i.e., the polarizations, displacements, and the potentials are initialized with small fluctuations around zero. For convenience of comparison between the different cases, the same initial random seed is used in all cases. The simulations were evolved until the domain pattern was stabilized; in the present case this was achieved within $t^* = 2\times10^7$ time steps. The minimal spatial scale of our numerical simulations δ was set equal to 1 nm. We have found this value to be small enough to describe the delicate features of the polarization modulations, e.g., ripples at the domain wall as seen in Figs. 1(e) and 1(f). The numerical results presented in the paper are carried out with a 128 × 128 nm^2 unit cell. To test if our results are cell-size sensitive, we have performed simulations at a few sizes and find no significant change in the domain patterns.

A. Coupling of polarization with shear strain gradients: f_{44}

Consider the case where the polarization is coupled only to shear strain gradients and the coupling to gradients of uniaxial strains is negligible. Simulations are performed for several values of the flexoelectric coefficient f_{44} along with the corresponding nonflexoelectric case $f_{44} = f_{12} = f_{11} = 0$. We first study the mechanically unconstrained case with $\langle\sigma_{xx}\rangle = \langle\sigma_{yy}\rangle = \langle\sigma_{xy}\rangle = 0$. Figures 1(a)–1(c) show the patterns for simulations run to $t^* = 2\times10^7$ time steps. The corresponding spatial variation of the polarizations in a horizontal cut across these images is shown in Figs. 1(d)–1(f). For all cases, the system develops a single ferroelastic variant with no 90° domain walls, as expected for a stress-free system. Figure 1(a) shows the pattern for the nonflexoelectric ($f_{44} = 0$) case where a single domain wall separates antiparallel ferroelectric polarizations. This pattern persists until $f_{44} = 5$ V. However, above $f_{44} = 5$ V, the number of domain walls in the patterns increases with increasing f_{44}. For $f_{44} \leqslant 12$ V, the polarization is homogeneous within each domain. At $f_{44} = 13$ V, along with coarse domains with homogeneous polarizations, very fine domains where the polarization within the domains is inhomogeneous also appear. We note that the characteristic feature of these domains is not their small size, but the

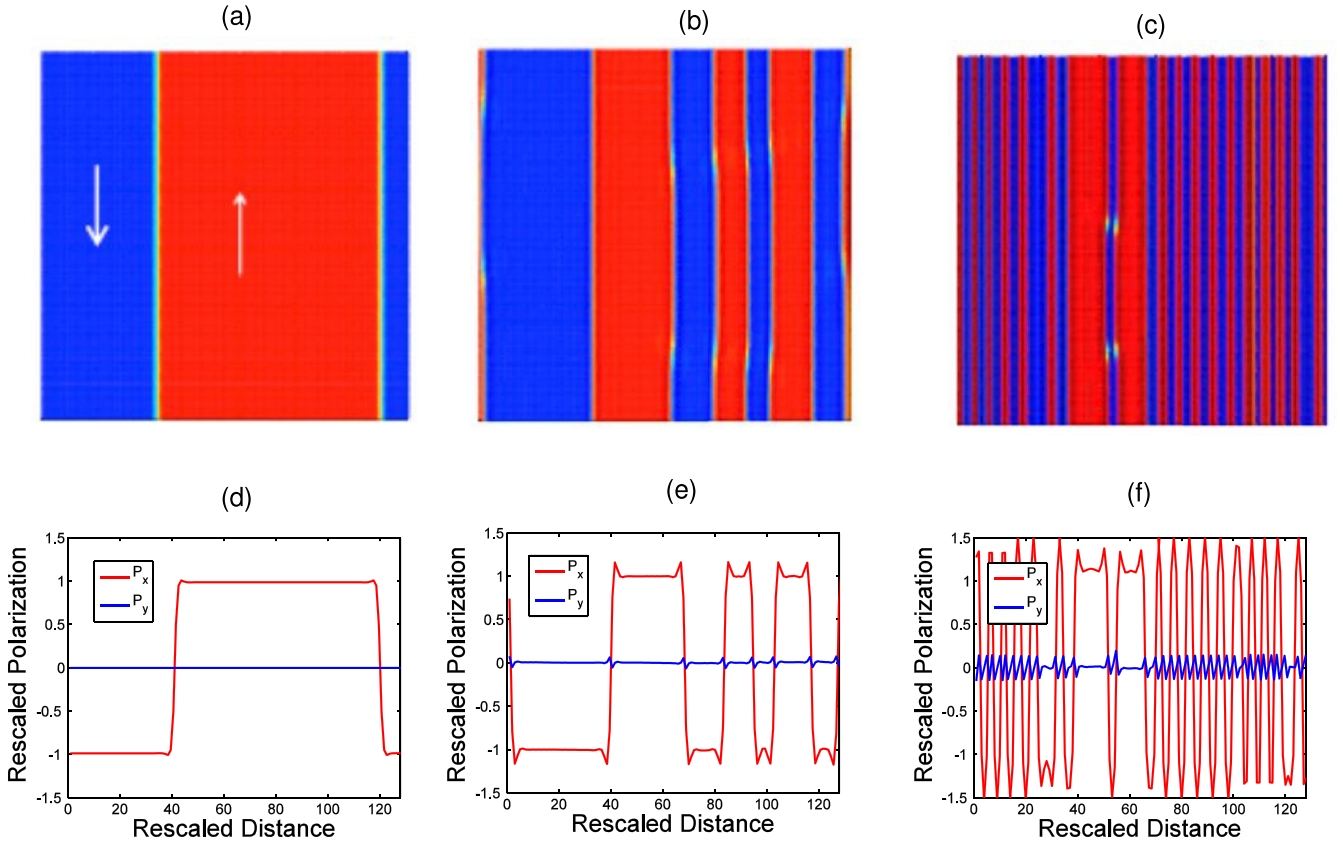

FIG. 1. (Color online) Domain patterns for the stress-free case, where the flexoelectric coupling f_{44} is increased from [(a) and (d)] 0 to [(b) and (e)] 12 V and then to [(c) and (f)] 15 V. Plots (a)–(c) show the x component of the polarization in the 128 × 128 nm^2 simulation cell. Polarization profiles (P_y/P_0 vs distance x/δ, along the simulation cell center) are shown for cases (a)–(c), in (d)–(f), respectively. $\delta = 1$ nm.

inhomogeneity of the polarization within the "domains" that makes them distinct from the coarser/homogeneous polarization domains. The polarization in these fine domains appears to have a nearly sinusoidal modulation of P_y along the x direction. This can be seen clearly in Fig. 1(f). These domains can be classified as "incommensurate" or modulated. The present simulation confirms that flexoelectricity can induce incommensurate phase formation in ferroelectrics, in agreement with Refs. [18–21]. Figures 1(d)–1(f) also show that the incommensurate domains can coexist with homogeneous polarization domains. As f_{44} increases, the fraction of the incommensurate domains increases at the expense of the homogeneous polarization domains. It is interesting to note that even when incommensurate phase domains do not form, "spikes" in polarizations are observed at the domain walls. The link between these spikes and the flexoelectric effect will be discussed in Sec. IV.

Figure 2 shows the patterns for the mechanically constrained case $\langle\varepsilon_{xx}\rangle = \langle\varepsilon_{yy}\rangle = \langle\varepsilon_{xy}\rangle = 0$. For the nonflexoelectric case, a domain pattern with two ferroelastic variants and with 90° uncharged (head to tail) domain walls is observed [Figs. 2(a) and 2(b)]. This pattern persists upon increasing f_{44} until $f_{44} = 5$ V. For $f_{44} > 5$ V we obtain states where there are antiparallel domains within the ferroelastic domains. Figures 2(c) and 2(d) show this four domain state pattern for $f_{44} = 7$ V. Note that at this value of f_{44}, the polarization is still homogeneous within the domains. Upon further increasing f_{44}, domains of the incommensurate phase also appear within the individual ferroelastic variants [see Figs. 2(e) and 2(f) for $f_{44} = 9$ V]. For $f_{44} = 12$ V a clear "herringbone" modulated pattern with fine antiparallel domains in each ferroelastically distinct variant is observed [Figs. 2(g) and 2(h)]. We note that such patterns were reported in single crystal $BaTiO_3$ in one of the earliest studies of ferroelectric domain patterns [30], albeit at much larger spatial scales.

B. Coupling of polarization with uniaxial strain gradients: f_{11}

Here we consider the case of flexoelectric coupling with gradient of the uniaxial strain along the polarization direction $f_{12} = f_{44} = 0$, $f_{11} \neq 0$. The simulated domain patterns for the stress-free boundary condition are shown in Fig. 3. The patterns are identical to the nonflexoelectric case for f_{11} up to 14 V [Fig. 3(a)]. This is quite different from the $f_{44} \neq 0$ case, where the number of domain walls increased with f_{44} even before the onset of the incommensurate phase. The observed difference in behavior between the f_{44} and f_{11} cases may be explained by the fact that the 180° polarization domain walls contain shear strain gradients, but do not contain uniaxial strain gradients. Equation (6) shows that the shear strain gradients $\partial u_{xy}/\partial x$ and $\partial u_{xy}/\partial y$ are coupled to the polarization via the f_{44} coefficient. Such coupling results in a reduction of the wall energy and leads to an increase in the density of domain walls. Meanwhile, f_{11} controls the coupling for

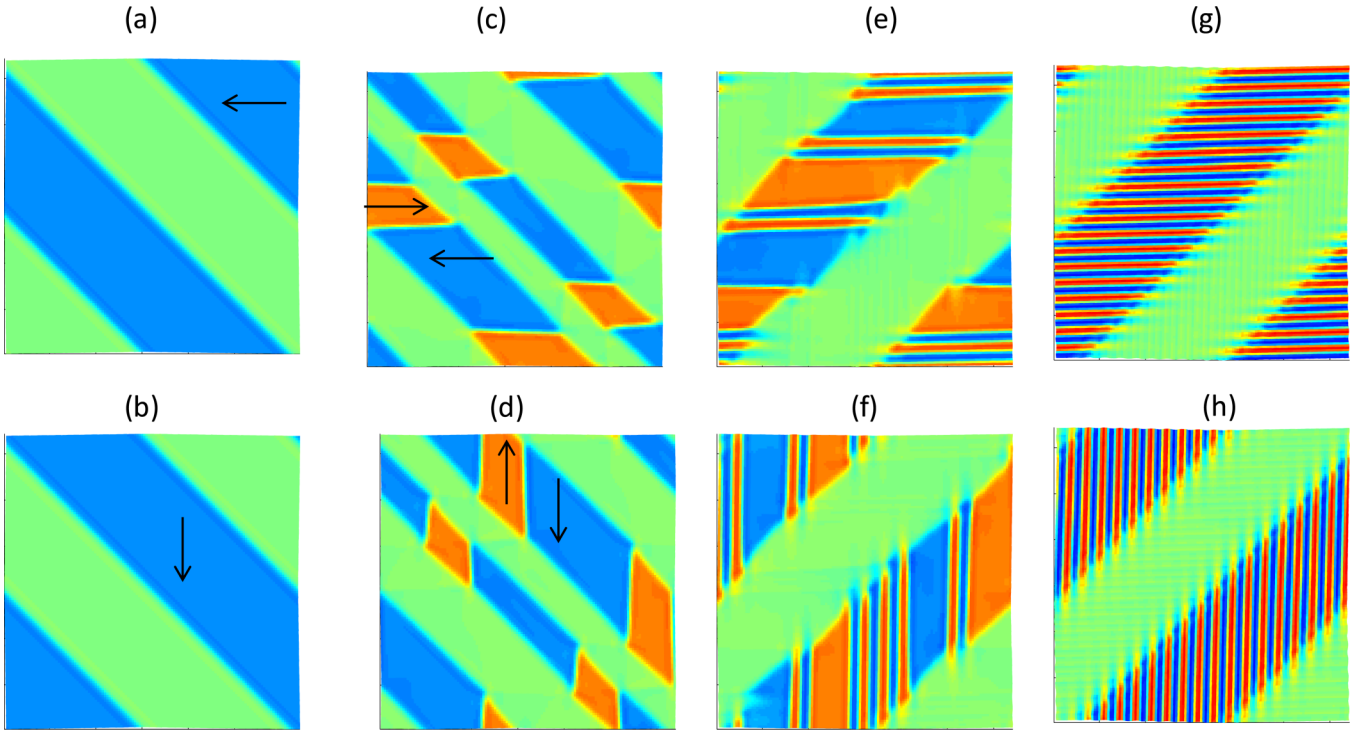

FIG. 2. (Color online) Domain pattern for the mechanically constrained case for different flexoelectric coupling strengths (a) and (b) $f_{44} = 0$, (c) and (d) $f_{44} = 7$ V, (e) and (f) $f_{44} = 9$ V, and (g) and (h) $f_{44} = 12$ V in the 128×128 nm^2 simulation cell. The top and bottom rows corresponds to the x and y components of the polarization, respectively.

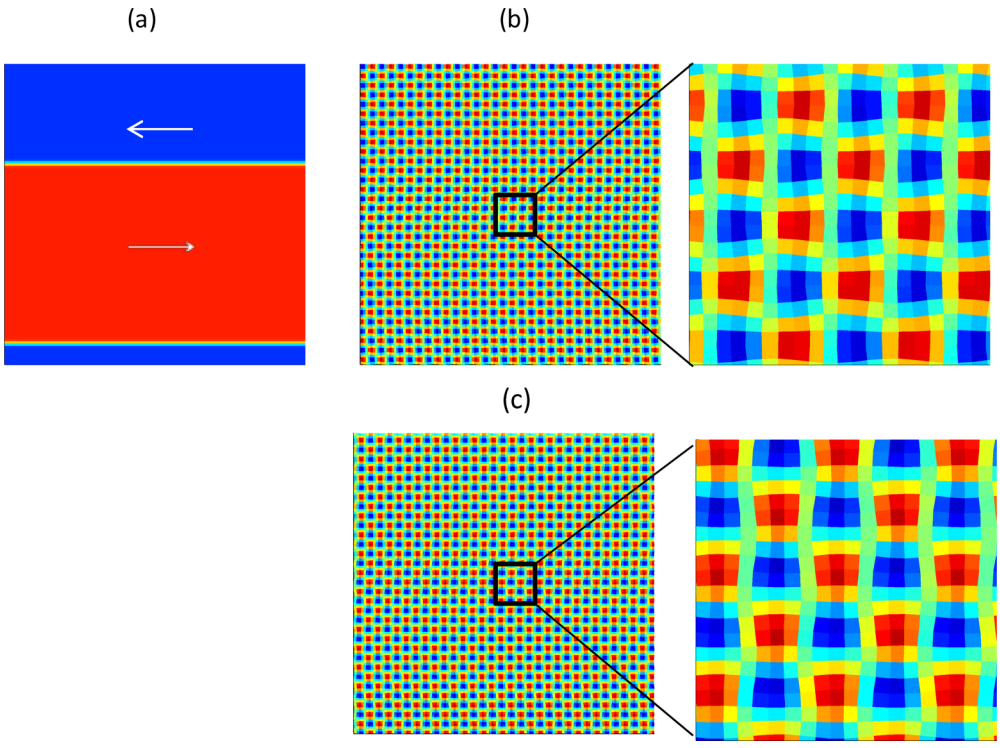

FIG. 3. (Color online) Domain pattern for the stress-free case when $f_{11} \neq 0$ for different flexoelectric coupling strengths. The nonvanishing components of the polarization are shown for each case. The patterns correspond to (a) $f_{11} = 14$ V (x-component of polarization) and (b) and (c) $f_{11} = 15$ V [(b) is the x component of polarization and (c) is the y component]. The size of the simulation cell is 128×128 nm^2. A magnified view of the polarization vectors for the regions indicated by the boxes are shown in Fig. 4.

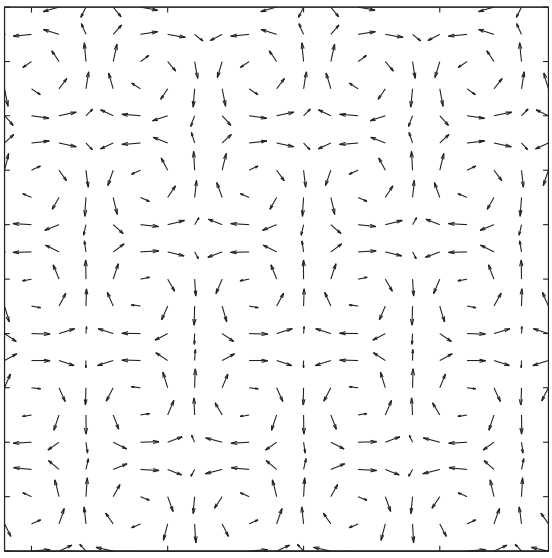

FIG. 4. The polarization vectors for the zoomed in region of Fig. 3.

uniaxial strain gradients $\partial u_{xx}/\partial x$ and $\partial u_{yy}/\partial y$, which are absent in domain walls that separate antiparallel polarization domains. This explains the insensitivity of the domain pattern to f_{11} in homogeneous polarization domains. The flexoelectric coupling related to the f_{11} coefficient reveals itself once f_{11} exceeds a critical value. At $f_{11} = 15$ V an unusual checkerboard pattern for both P_x and P_y is formed, as seen in Figs. 3(b) and 3(c). This is also a transition from a ferroelectric domain pattern to a modulated/incommensurate state. This two-dimensional modulation is significantly different from those seen for $f_{44} \neq 0$ in Fig. 1. To display the 2D structure of the modulation, a magnified view of the polarization distributions for $f_{11} = 15$ V is also shown in Fig. 4. This figure shows that the modulated pattern is actually an array of localized polarization vortices, where neighboring vortices have opposite chirality. There has been much discussion in the literature about the existence of polarization vortices in ferroelectrics. It is known that both stripe patterns and vortex structures form to minimize electrostatic energy of a finite sample. In the classical ferroelectric situation, the vortex structure better minimizes the electrostatic energy, but has a higher energy per unit volume in comparison with the stripe pattern, thus it was predicted to appear only in very small (nanometer-scale) samples [31,32]. Naively, one might think that in our case the explanation for the appearance of this structure is similar because we deal with a sample of only a 128 × 128 nm^2 sample. However, because the present simulations were performed with periodic boundary conditions, our sample is effectively of infinite extent (hence, this electrostatic-related explanation cannot be applied to our case). The simulated vortex array is a result of the combined action of the flexoelectric effect, the effects of anharmonicities, and anisotropy of the system, as will be elucidated in Sec. IV.

Next, we turn to the corresponding mechanically constrained case, for which Fig. 5 shows the domain patterns. Figure 6 shows a magnified view of the polarization vectors in representative regions. The domain patterns remain similar to the nonflexoelectric case shown in Figs. 2(a) and 2(b) until $f_{11} = 8$ V. When $f_{11} = 8$ V, one observes formation of an additional narrow ferroelastic domain [Figs. 5(a) and

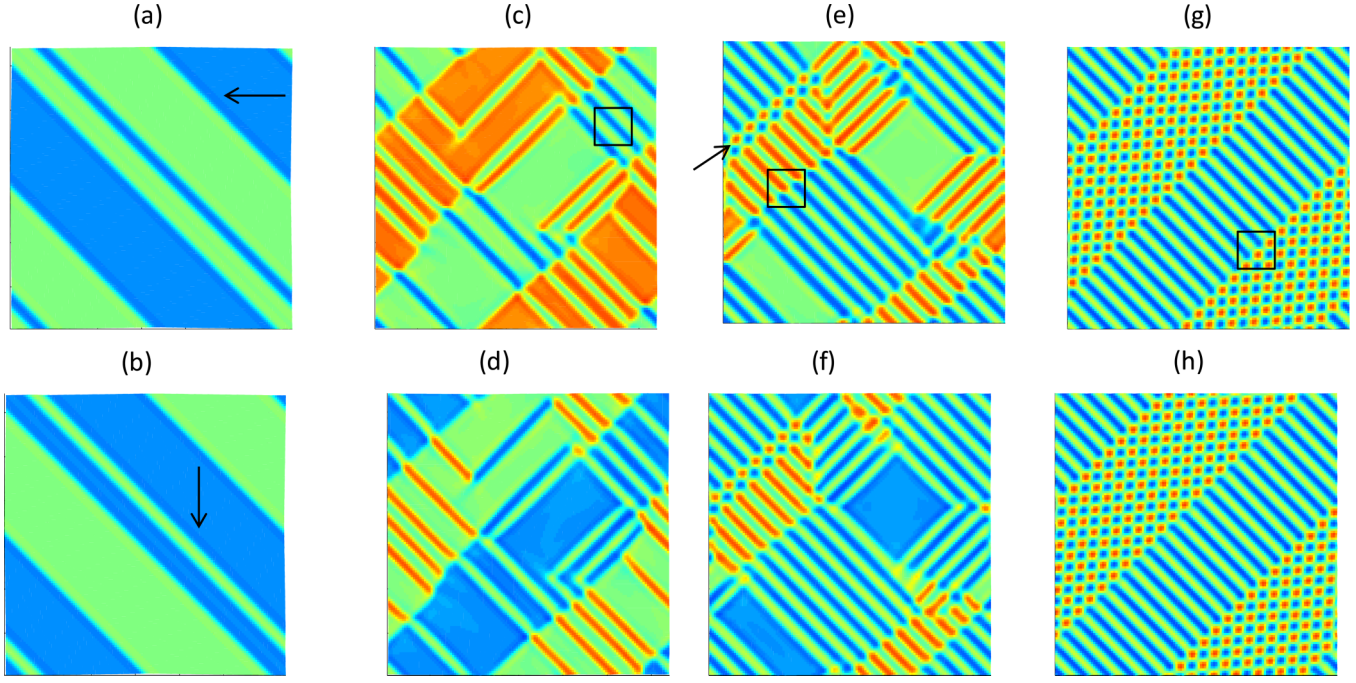

FIG. 5. (Color online) Domain patterns for the mechanically constrained case when $f_{11} \neq 0$ for different flexoelectric coupling strengths. Both the x and y components of the polarization are shown for each case. The top row corresponds to the x component and the bottom row corresponds to the y component. The patterns correspond to (a) and (b) $f_{11} = 8$ V, (c) and (d) $f_{11} = 10$ V, (e) and (f) $f_{11} = 11$ V, and (g) and (h) $f_{11} = 12$ V. The polarization distribution for the marked regions is shown in Fig. 6(a) for $f_{11} = 10$ V, Fig. 6(b) for $f_{11} = 11$ V, and Fig. 6(c) for $f_{11} = 12$ V. The size of the simulation cell is 128 × 128 nm^2.

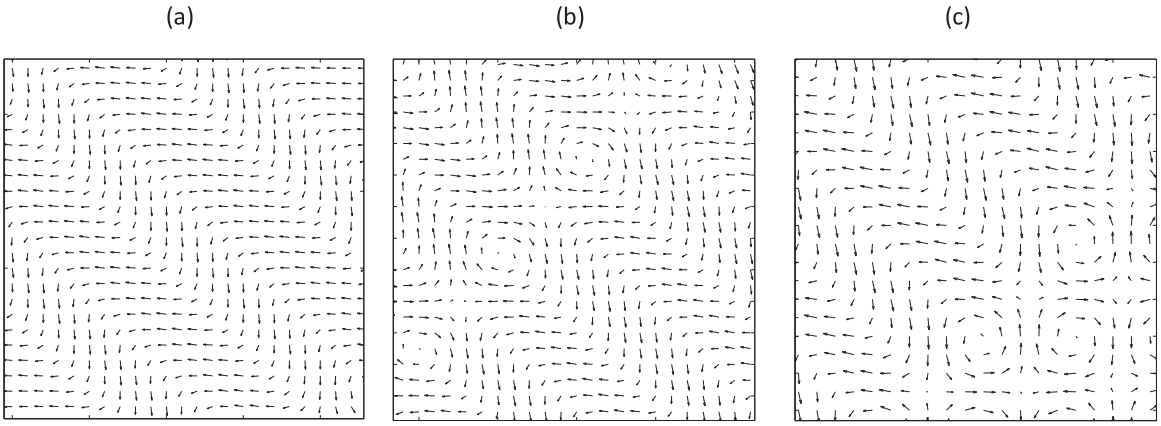

FIG. 6. Magnified view of the polarization distributions for the marked regions in Fig. 5.

5(b)]. For $f_{11} > 8$ V, the density of the 90° domain walls increases with increasing f_{11}. This situation is different than in the mechanically free sample, where the population of the domain walls was insensitive to the value of f_{11}. This can be readily understood in view of the oblique orientations of the 90° domain walls. In such walls, the gradients of the strain component u_{xx} and u_{yy} (coupled to the f_{11} coefficient) are present. Thus, the wall energy becomes sensitive to the value of this coefficient, thereby affecting the wall population.

The domain pattern drastically changes for $f_{11} = 10$ V [Figs. 5(c) and 5(d)]. All four variants are present in this case and a very fine 90° domain structure appears. This fine domain pattern coexists with domains having homogeneous polarizations. A magnified view of the region in the box in that figure is shown in Fig. 6(a). By plotting polarization profiles, similar to those in Fig. 1, we have confirmed that the fine-stripe domains in Fig. 5 are modulated with nonuniform polarizations within the domains. Thus, here we observe an "intermediate" one-dimensional modulated phase, which was not encountered in the stress-free case. For $f_{11} = 11$ V [Figs. 5(e) and 5(f)] we observe four different types of domains of this one-dimensional modulated phase: the initial one, the one rotated by 90°, and two additional ones that are shifted by a half-period. These domains coexist with the homogeneous polarization domains as well as a small fraction of the two-dimensional modulated structure similar to the checkerboard pattern observed in the stress-free case. The domain walls between the two different domains of the 1D modulated structure are interesting and unusual; see, e.g., the region inside the box in the image for $f_{11} = 11$ V for which the polarization vectors are shown in Fig. 6(b). We can see that the domain wall represents a row of polarization vortices. These vortices are precusors to the formation of the 2D modulated phase. As can be seen, in some regions, such a domain wall may be replaced by a thin stripe of the 2D modulated structure [indicated by the arrow in Fig. 5(e)]. We should remark that such domain walls have been observed in recent experiments on free standing PZT nanostructures [33]. Further increase of f_{11} leads to the growth of the 2D modulated structure at the expense of homogeneous polarization domains. For $f_{11} = 12$ V the homogeneous polarization domains disappear. The 2D vortex array pattern grows and coexists with the 1D modulated pattern [Figs. 5(g) and 6(h)]. Figure 6(c) shows the local polarization distribution for a typical region at an interface of the coexisting patterns. At higher flexoelectric coupling values ($f_{11} \geqslant 13$ V), the entire system is in the 2D modulated phase, similar to that shown in Fig. 3 for the case $f_{11} = 15$ V.

We also studied the $f_{11} = f_{44} = 0$, $f_{12} \neq 0$ case. This case represents the coupling of the polarization with the gradient of the other component of the uniaxial strain than considered above. For the stress-free sample, the obtained patterns are identical to those in the case $f_{11} \neq 0$. For the mechanically constrained sample, while the generic features of the patterns are the same as for the case with $f_{11} \neq 0$, the critical values for the onset of the 2D modulated phase are slightly different.

IV. ANALYTICAL TREATMENT AND DISCUSSION OF SIMULATION RESULTS

To gain additional insight into the patterns obtained from the simulations, we provide a theoretical treament of these results. Our aim is to find the critical values of the flexocoupling coefficients required for incommensurate phases to form, rationalizing the observed orientations of the modulation wave vectors, and explain the occurrence of the 2D modulated structure.

A. Instability with respect to the formation of the modulated state

Though our simulations have been performed for parameters corresponding to the ferroelectric phase, the information about the orientation of the wave vectors of possible modulated structures can be obtained from the analysis of the stability of the paraelectric phase with respect to the modulations. Such an analysis can also provide an estimate for the modulated phase formation condition.

Once a ferroelectric material approaches the Curie temperature upon cooling, the phase transition into a homogeneous ferroelectric phase occurs [18] unless the system becomes unstable with respect to spatial modulations with a finite wave vector $\vec{k}_{\min}$. When such an instability is observed, the phase transition occurs into a modulated phase. The instability with respect to the formation of spatial modulations can be checked by analyzing the linearized equations of state for the polarization and mechanical degrees of freedom. Such

equations follow from the equilibrium condition, whereby the left-hand sides of Eqs. (12) and (13) are set to zero. Rewriting these equations in terms of displacements, using Eqs. (7), (8), and (13), and linearizing them one obtains

$$
\begin{aligned}
&2\alpha_1 P_x - f_{11}\left(\frac{\partial^2 u_x}{\partial x^2}\right) - f_{12}\left(\frac{\partial^2 u_y}{\partial x \partial y}\right) - f_{44}\left(\frac{\partial^2 u_x}{\partial y^2} + \frac{\partial^2 u_y}{\partial x \partial y}\right) - \lambda_1 \nabla^2 P_x + \lambda_2 \nabla^2(\nabla^2 P_x) + \frac{\partial \varphi}{\partial x} = 0,\\
&2\alpha_1 P_y - f_{11}\left(\frac{\partial^2 u_y}{\partial y^2}\right) - f_{12}\left(\frac{\partial^2 u_x}{\partial x \partial y}\right) - f_{44}\left(\frac{\partial^2 u_y}{\partial x^2} + \frac{\partial^2 u_x}{\partial x \partial y}\right) - \lambda_1 \nabla^2 P_y + \lambda_2 \nabla^2(\nabla^2 P_y) + \frac{\partial \varphi}{\partial y} = 0,\\
&C_{11}\frac{\partial^2 u_x}{\partial x^2} + C_{12}\frac{\partial^2 u_y}{\partial x \partial y} + C_{44}\frac{\partial^2 u_x}{\partial y^2} + C_{44}\frac{\partial^2 u_y}{\partial x \partial y} + \left[f_{11}\frac{\partial^2 P_x}{\partial x^2} + f_{12}\frac{\partial^2 P_y}{\partial x \partial y} + f_{44}\left(\frac{\partial^2 P_x}{\partial y^2} + \frac{\partial^2 P_y}{\partial y \partial x}\right)\right] = 0,\\
&C_{11}\frac{\partial^2 u_y}{\partial y^2} + C_{12}\frac{\partial^2 u_x}{\partial x \partial y} + C_{44}\frac{\partial^2 u_y}{\partial x^2} + C_{44}\frac{\partial^2 u_x}{\partial x \partial y} + \left[f_{11}\frac{\partial^2 P_y}{\partial y^2} + f_{12}\frac{\partial^2 P_x}{\partial x \partial y} + f_{44}\left(\frac{\partial^2 P_y}{\partial x^2} + \frac{\partial^2 P_x}{\partial y \partial x}\right)\right] = 0.
\end{aligned}
\tag{14}
$$

The paraelectric state $P_x = P_y = u_x = u_y = 0$ is clearly a solution to Eq. (14). To investigate the stability of the paraelectric state, one introduces an infinitesimal perturbation, given as $P_i(\vec{r}) = \int \tilde{P}_i(\vec{k}) e^{i\vec{k}\cdot\vec{r}} d\vec{k}$, $u_i(\vec{r}) = \int \tilde{u}_i(\vec{k}) e^{i\vec{k}\cdot\vec{r}} d\vec{k}$, and $\phi(\vec{r}) = \int \tilde{\phi}(\vec{k}) e^{i\vec{k}\cdot\vec{r}} d\vec{k}$. Substituting these in Eq. (14), we can express (14) in terms of Fourier components as $\hat{M}\vec{V} = 0$, where

$$
\hat{M} = \begin{pmatrix}
a(k) + \frac{k_x^2}{k^2 \varepsilon_b} & \frac{k_x k_y}{k^2 \varepsilon_b} & \left(f_{11}k_x^2 + f_{44}k_y^2\right) & k_x k_y (f_{12} + f_{44}) \\
\frac{k_x k_y}{k^2 \varepsilon_b} & a(k) + \frac{k_y^2}{k^2 \varepsilon_b} & k_x k_y (f_{12} + f_{44}) & \left(f_{11}k_y^2 + f_{44}k_x^2\right) \\
\left(f_{11}k_x^2 + f_{44}k_y^2\right) & k_x k_y (f_{12} + f_{44}) & C_{11}k_x^2 + C_{44}k_y^2 & k_x k_y (C_{12} + C_{44}) \\
(f_{12} + f_{44}) k_x k_y & \left(f_{11}k_y^2 + f_{44}k_x^2\right) & k_x k_y (C_{12} + C_{44}) & C_{11}k_y^2 + C_{44}k_x^2
\end{pmatrix},
\tag{15a}
$$

$$
\vec{V} = \begin{pmatrix} \tilde{P}_x \\ \tilde{P}_y \\ \tilde{u}_x \\ \tilde{u}_y \end{pmatrix},
\tag{15b}
$$

where $a(k) = 2\alpha_1 + \lambda_1 k^2 + \lambda_2 k^4$. Here the Fourier transform of the electrostatic potential $\phi(\vec{k}) = -i\frac{\vec{k}\cdot\vec{P}}{\varepsilon_b k^2}$ is used, which follows from Eq. (10). In deriving (15) we have used the fact that $\frac{\partial^2 \phi}{\partial x_i \partial x_j} \rightarrow -k_i k_j \phi(\vec{k})$ in terms of Fourier components.

In view of the linearity of the problem, one may consider the stability with respect to each Fourier component independently. Critical modes (perturbations having lowest energies) may be found from the following eigenvalue problem:

$$
\hat{M}\vec{V} = \omega \vec{V}.
\tag{16}
$$

The paraelectric phase is stable if all four eigenvalues ω in (16) are positive for all $\vec{k}$. If one of the eigenvalues becomes negative, this implies that the modulated phase becomes energetically favorable and will imply transition into the incommensurate phase. The modulated phase may be reached by decreasing the temperature or by increasing the magnitude of the flexoelectric coupling. Since the eigenvalues of Eq. (16) depend on the magnitude and orientation of the wave vector of the modulation, the transition will first occur for some critical wave vector $\vec{k} = \vec{k}_{\min} \neq 0$. Thus, the criterion for the transition into the modulated phase is the change of sign of the lowest eigenvalue for the critical wave vector $\vec{k} = \vec{k}_{\min} \neq 0$ from positive to negative. The "natural" directions for the critical vectors are $\langle 01 \rangle$ and $\langle 11 \rangle$ as given by the symmetry of the material. In Appendix B it is shown that, in our system, the critical vectors should indeed belong to these high symmetry crystallographic directions.

The expressions for the minimal eigenvalue ω_- in these two cases have the form (see Appendix B)

$$
\omega_-(01) = \alpha + k^2\left(\lambda_1 - \frac{f_{44}^2}{C_{44}}\right) + k^4\lambda_2
\tag{17}
$$

for the $\langle 01 \rangle$ directions and

$$
\omega_-(11) = \alpha + k^2\left[\lambda_1 - \frac{(f_{11} - f_{12})^2}{2(C_{11} - C_{12})}\right] + k^4\lambda_2
\tag{18}
$$

for the $\langle 11 \rangle$ directions.

Analysis of Eq. (17) allows us to readily check that when

$$
f_{44}^2 > \lambda_1 C_{44},
\tag{19}
$$

as we approach the ferroelectric instability at $\alpha = 0$, the system can become unstable with respect to a modulation with a wave vector parallel to a $\langle 01 \rangle$ direction. The analysis of Eq. (18) suggests such an instability with respect to a wave vector parallel to a $\langle 11 \rangle$ direction occurs if

$$
(f_{11} - f_{12})^2 > 2\lambda_1(C_{11} - C_{12}).
\tag{20}
$$

Thus, Eqs. (19) and (20) imply that if the flexocoupling coefficients are sufficiently large, the system becomes potentially unstable with respect to the occurrence of modulated states with critical wave vectors parallel to the $\langle 01 \rangle$ or $\langle 11 \rangle$ directions. Which state will actually occur may be answered by comparing the magnitudes of $\omega_-(01)$ and $\omega_-(11)$ using Eqs. (17) and (18). Such a comparison shows that the critical wave vectors

will be in the ⟨01⟩ directions if

$$f_{44}^2 > \frac{C_{44}\,(f_{11}-f_{12})^2}{2\,(C_{11}-C_{12})} \tag{21}$$

or the ⟨11⟩ directions otherwise.

Applying Eq. (21) to the cases covered by our numerical simulations one concludes that for $f_{12}=f_{11}=0,\ f_{44}\neq 0$ the modulation vector should be parallel to the ⟨01⟩ direction, while for $f_{12}=f_{44}=0,\ f_{11}\neq 0$ to the ⟨11⟩. One can also infer that, for $f_{11}=f_{44}=0,\ f_{12}\neq 0$, the situation should be similar to the case $f_{12}=f_{44}=0,\ f_{11}\neq 0$. The modulation direction in the $f_{12}=f_{11}=0,\ f_{44}\neq 0$ case is consistent with the results of our simulations, shown in Figs. 1 and 2. As for the $f_{12}=f_{44}=0,\ f_{11}\neq 0$ and $f_{11}=f_{44}=0,\ f_{12}\neq 0$ cases, where 2D patterns were obtained in simulations, the consistency will be demonstrated in the next subsection, where it will be shown that the 2D patterns may be viewed as a superposition of two linear modulations having ⟨11⟩ directions of the wave vectors.

Using Eqs. (19) and (20) and the numerical parameters of the model one can evaluate the critical (for the occurrence of the modulated phase) values of the flexocoupling coefficients as $f_{11}^{\rm cr}=5.3$ V and $f_{44}^{\rm cr}=4$ V. These values agree, to within an order of magnitude, with the threshold values for the formation of the modulated phase in the simulations. However, a more detailed comparison of these parametes is not possible since the case in which the modulated phase dominates the homogeneous state in the ferroelectric phase is controlled by not only the strength of the incommensurate instability [via Eqs. (19) and (20)] but also by anharmonic effects not accounted for in the linear analysis presented above.

B. Role of anharmonicity: Occurrence of 2D modulated pattern

A remarkable feature of the results of our simulations is that the occurrence of 1D or 2D modulations in the incommensurate phase depends on which of the flexocoupling coefficients come into play. Here we elucidate this feature using the results of the analysis presented above and incorporating the efffect of the lattice anharmonicity.

The above analysis predicts that once the flexoelectric coefficients exceed a critical value, modulated patterns will develop. Once the modulated state occurs, its modulation wave vector can acquire one of the four possible, energetically degenerate, orientations. Thus, we see that linear analysis cannot specify the polarization state which will form below the phase transition, since any linear combination of these polarization states will have the same energy. As often happens in similar situations in the theory of phase transitions, the polarization state is contolled by anharmonic and crystalline anisotropy effects.

In the analysis below we will demonstrate how the tetragonal anharmonicities of the model examined in our simualtions can lead to 1D modulations for $f_{12}=f_{11}=0,\ f_{44}\neq 0$ and to 2D modulations for $f_{12}=f_{44}=0,\ f_{11}\neq 0$. We will do this in the simplest approximation, neglecting the elastic contributions to the anharmonicities and taking into account only the fourth-power terms in the polarization. Thus we consider the anharmonic contribution to the free energy in the form

$$f_s=\alpha_{11}\left(P_x^4+P_y^4\right)+\alpha_{12}P_x^2P_y^2\,, \tag{22}$$

where $\alpha_{11}>0$ and $\alpha_{12}>-2\alpha_{11}$ to ensure the stability of the system. Equation (22) suggests that, in the case of homogeneous ferroelectric state, the tetragonal phase is energetically favorable if

$$\alpha_{12}>2\alpha_{11}\,, \tag{23}$$

otherwise it represents the orthorhombic state.

In the case where $f_{12}=f_{11}=0,\ f_{44}\neq 0$, as shown above, the possible modulations are controlled by the wave vectors ($k_x=\pm k_{\rm min},\ k_y=0$) and ($k_x=0,\ k_y=\pm k_{\rm min}$). The corresponding polarization profiles can be presented in the form

$$\begin{pmatrix}P_x\\P_y\end{pmatrix}=A\cos(k_{\rm min}y)\begin{pmatrix}1\\0\end{pmatrix}=A\vec{m}_1, \tag{24}$$

$$\begin{pmatrix}P_x\\P_y\end{pmatrix}=B\cos(k_{\rm min}y)\begin{pmatrix}0\\1\end{pmatrix}=A\vec{m}_2, \tag{25}$$

where A and B are the amplitudes of the modulations. To predict which linear combination of the degenerate solutions in (24) and (25) describes the modulated state, one can take advantage of the smallness of the amplitude of the appearing modulated profile by applying perturbation theory for the degenerate states (like one does in quantum mechanics). Specifically we will calculate the anharmonic energy for a linear combination of the degenerate solutions and minimize it with respect to the mixing coefficients.

Thus we consider a normalized linear combination of the modulations in Eqs. (24) and (25):

$$\vec{m}=A\vec{m}_1+B\vec{m}_2,\quad A^2+B^2=1. \tag{26}$$

Note that we do not incorporate a possible phase shift between solutions (24) and (25) since it does not affect the energy of the system, leading to a possible spatial translation of the polarization distribution.

Substitution of (26) into (22) and averaging over the modulation period yields

$$\langle f_s(\vec{m})\rangle=\tfrac{3}{8}\alpha_{11}+\tfrac{1}{4}(3\alpha_{11}-\alpha_{12})A^2(A^2-1), \tag{27}$$

where $0\leqslant A^2\leqslant 1$. Minimization of (27) with respect to A^2 gives

$$A^2=0,\quad B^2=1\quad\text{or}\quad A^2=1,\quad B^2=0, \tag{28a}$$

if

$$\alpha_{12}>3\alpha_{11} \tag{28b}$$

and

$$A^2=B^2=1/2 \tag{28c}$$

if

$$\alpha_{12}<3\alpha_{11}\,. \tag{28d}$$

We note that inequality (28b) implies the inequality (23) for the formation of the tetragonal phase. Thus, in the frame of our model, a situation where there is no mixing between solutions (24) and (25) is possible only when the tetragonal phase is preferred over the orthorhombic one in the material.

This mixing will occur in the orthorhombic phase and in the tetragonal one for weak tetragonality (i.e., $3\alpha_{11} > \alpha_{12} > 2\alpha_{11}$), as controlled by Eqs. (28c) and (28d). In the numerical simulations, solutions (24) and (25) were seen individually, but not their linear combinations (Figs. 1 and 2), which agrees with the analytical predictions for the case of sufficiently large tetragonality.

A similar analysis can be performed for the $f_{12} = f_{44} = 0$, $f_{11} \neq 0$ case, where the modulation wave vector is in the $\langle 11 \rangle$ directions. Here the problem may be reduced to the one just considered, using a reference frame tilted to 45°, where $x_1 = \frac{x+y}{\sqrt{2}}$, $x_2 = \frac{x-y}{\sqrt{2}}$, P_1 and P_2 are polarization components along x_1 and x_2 correspondingly, and the possible modulations are

$$\begin{pmatrix} P_1 \\ P_2 \end{pmatrix} = A\cos(k_{\min} x_2) \begin{pmatrix} 1 \\ 0 \end{pmatrix} = A\vec{m}_3, \tag{29}$$

$$\begin{pmatrix} P_1 \\ P_2 \end{pmatrix} = B\cos(k_{\min} x_2) \begin{pmatrix} 0 \\ 1 \end{pmatrix} = B\vec{m}_4, \tag{30}$$

which is identical to (25) and (26). In the $\{x_1,x_2\}$ reference frame, the potential (23) takes the form

$$f_s = \left(\frac{2\alpha_{11} + \alpha_{12}}{4}\right)\left(P_1^4 + P_2^4\right) + \left(\frac{6\alpha_{11} - \alpha_{12}}{2}\right) P_1^2 P_2^2, \tag{31}$$

implying that above results (28) may be used with the substitution $\alpha_{11} \to \frac{2\alpha_{11}+\alpha_{12}}{4}$; $\alpha_{12} \to \frac{6\alpha_{11}-\alpha_{12}}{4}$.

For this case, one obtains

$$A^2 = 0, \quad B^2 = 1 \quad \text{or} \quad A^2 = 1, \quad B^2 = 0 \tag{32a}$$

if

$$\alpha_{12} < 1.2\alpha_{11} \tag{32b}$$

and

$$A^2 = B^2 = 1/2 \tag{32c}$$

if

$$\alpha_{12} > 1.2\alpha_{11}. \tag{32d}$$

For the case where the homogeneous state is tetragonal, $\alpha_{12} > 2\alpha_{11}$. Thus, Eq. (32d) is trivially met, and the half-sum of the modulations (29) and (30) will be preferred. In the initial reference frame, this gives rise to a polarization distribution

$$\begin{aligned} P_x &= A\cos(k_{\min} x/\sqrt{2})\cos(k_{\min} y/\sqrt{2})/\sqrt{2}, \\ P_y &= A\sin(k_{\min} x/\sqrt{2})\sin(k_{\min} y/\sqrt{2})/\sqrt{2}. \end{aligned} \tag{33}$$

Figure 7 shows the vector plot associated with the polarization components given by Eq. (33). Note the vortex arrays which are similar to those obtained in the simulations (see Figs. 3 and 4). Thus the 2D vortex array can be viewed as a superposition of two 1D modulations.

Summarizing the results of the above analysis, one can formulate general conditions for the formation of 2D pattern. One can distinguish two situations: (i) The modulation wave vector makes an angle of 45° with one of the directions preferred by the polarization for the homogeneous ferroelectric state and (ii) the modulation wave vector is along one of the directions preferred by the polarization for the homogeneous ferroelectric state. Specifically, in the "tetragonal" system (i.e., for $\alpha_{12} > 2\alpha_{11}$), situation (i) takes place for the $\langle 11 \rangle$ modulation direction, while situation (ii) applies in the $\langle 01 \rangle$ modulation direction. One concludes that situation (i) always corresponds to the 2D modulated pattern. At the same time, in situation (ii) the 1D pattern will form only under the condition that the anisotropy of the system is strong enough, while for relatively weak anisotropy ($3\alpha_{11} > \alpha_{12} > 2\alpha_{11}$ for tetragonal and $2\alpha_{11} > \alpha_{12} > 1.2\alpha_{11}$ for orthorhombic systems) the 2D modulated pattern will form.

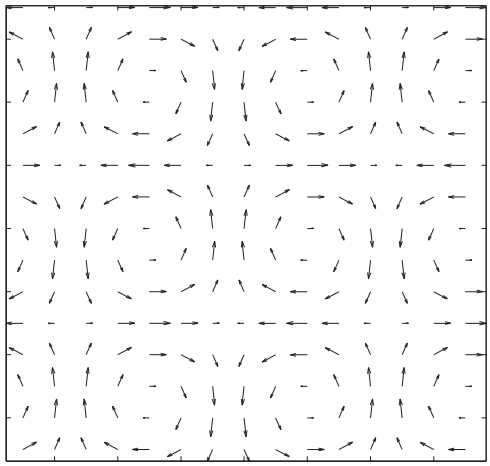

FIG. 7. Magnified view of the polarization vectors for the modulation given by Eq. (33).

The above analysis corroborates the observations made on the basis of the simulations. The model treated in our simulations has tetragonal anisotropy so that the $f_{12} = f_{44} = 0$, $f_{11} \neq 0$ case with the $\langle 11 \rangle$ modulation directions corresponds to situation (i), while the $f_{12} = f_{11} = 0$, $f_{44} \neq 0$ case corresponds to situation (ii). Thus, the simulated 2D pattern for $f_{12} = f_{44} = 0$, $f_{11} \neq 0$ perfectly matches the prediction of our analysis. The 1D patterns observed in the $f_{12} = f_{11} = 0$, $f_{44} \neq 0$ simulations are also consistent with our analytical predictions on the assumption that the tetragonality of the model is sufficiently large.

C. Impact of flexoelectric effect on the polarization profile in domain walls

As follows from the numerical simulations, even if the flexoelectric coupling is not sufficiently strong to drive the material into an incommensurate phase, there is still some impact of the effect on the structure and density of domain walls (see, e.g., Fig. 1). Here we analyze this effect with the framework of our simplified theoretical model. We consider the polarization profile in 180° [01]-oriented domain walls. To see clearer the impact of the flexoelectricity, we take into acount among the electromechanical couplings only the flexoelectricity. As follows from Eq. (17), the flexoelectric coupling results in renormalization of the correlation term $\lambda_1^{(\text{eff})} = \lambda_1 - \frac{f_{44}^2}{C_{44}}$. In our simple model the polarization can

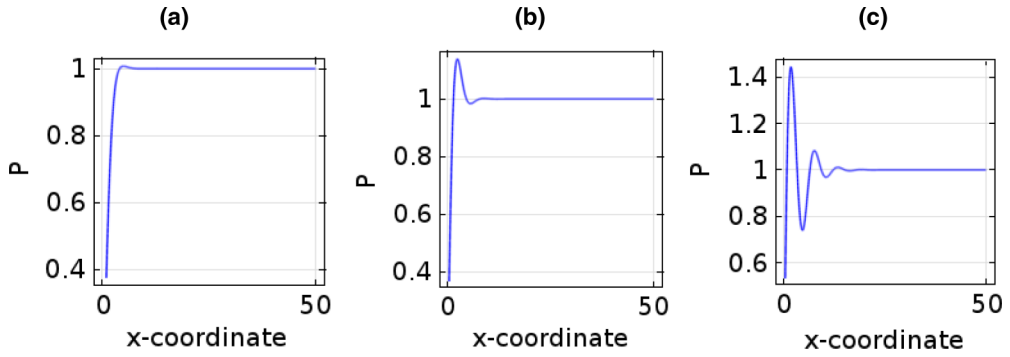

FIG. 8. (Color online) Development of the spikes in the polarization profile of the domain walls with increase of the flexocoupling coefficient. Solutions of Eq. (35) for (a) $l = -1$, (b) $l = 1$, and (c) $l = 2.3$.

be found as a solution to the equation

$$\alpha P + \beta P^3 + P''\left(\lambda_1 - \frac{f_{44}^2}{C_{44}}\right) + \lambda_2 \mathrm{P}'''' = 0. \qquad (34)$$

Here P'' refers to second-order spatial derivative and P'''' is the fourth-order spatial derivative. Analysis of equations of this type in the context of ferroics was performed in Ref. [27]. Equation (34) can be rewritten in dimensionless form as

$$-p + p^3 + lp'' + \mathrm{p}'''' = 0, \quad p = P/P_s, \quad \xi = \frac{x}{(\lambda_2/\alpha)^{1/4}},$$

$$l = \left(\frac{\lambda_1 - \frac{f_{44}^2}{C_{44}}}{\sqrt{\alpha\lambda_2}}\right), \qquad (35)$$

where "′" stands for derivative with respect to ξ. The shape of the polarization profile is controlled by a single parameter l. Equation (35) can be solved numerically to predict the behavior of the polarization. Figure 8 shows the solutions of Eq. (35) for a single domain wall. It is clear that spikes develop at domain walls as l is increased via the increase of the flexocoupling. This simple analysis explains the growth of polarization spikes with increase of flexocoupling observed in the simulations (Fig. 1). Thus it is demonstrated that flexoelectric effects can significantly influence the domain walls in ferroelectrics, even when the incommensurate phase does not form. For more detailed analysis of the formation of modulated structures starting from domain walls the reader is referred to work [27].

V. SUMMARY AND CONCLUSIONS

We have revisited the nature of ferroelectric domains, taking into account the flexoelectric coupling using both phase field simulations and analytical theory. We studied bulk domain patterns in cubic to tetragonal ferroelectrics with a 2D model. Since the thermodynamic fluctuations do not seem to play any appreciable role in the problems addressed, the 2D character of the model should not introduce any artifacts. Meanwhile, some domain configurations possible in the 3D world may be missing from our analysis. Thus, in addition to the effects identified in the paper, more involved phenomena may occur due to flexoelectricity in real 3D crystals.

To understand the effect of each component of the flexoelectric tensor, we have separately analyzed the $f_{12} = f_{44} = 0$, $f_{11} \neq 0$ and $f_{12} = f_{11} = 0$, $f_{44} \neq 0$ cases. Complex patterns in each case upon increasing the strength of the flexoelectric coupling were obtained. These patterns are very sensitive to the value of the flexoelectric coupling constants. For example, in Figs. 1–6 the domain patterns change significantly by changing the coupling constants by just 1 V. This clearly highlights the need for accurate determination of the flexoelectric coefficients. We also find that in both cases there is a critical value of f_{ij} above which modulated phases form with both polarization and strain gradients. The inhomogeneous distribution of the polarization depends on which component of f_{ij} is nonzero. For example, when the polarization is coupled to shear strain gradients ($f_{44} \neq 0$), a stripe modulation with antiparallel polarization is observed. For the mechanically constrained case, a "herringbone" domain pattern with antiparallel polarization domains within each ferroelastic variant is obtained, reminiscent of domain patterns observed in $BaTiO_3$ [30] (though with a different spatial scale). When the polarizations are coupled to gradients in the uniaxial strains ($f_{11} \neq 0$ or $f_{12} \neq 0$), a 2D checkerboard modulation of the polarization is obtained. This modulation corresponds to an array of localized polarization vortices, where neighboring vortices have opposite senses. Polarization vortices are usually believed to arise due to electrostatic effects; however, we have shown that flexoelectricity can also lead to localized polarization vortices.

To further understand the patterns observed in simulations, we addressed the system using an analytical treatment. This treatment allows us to predict the possible orientations of the modulation wave vectors in the incomensurate phase and indicates which orientations will be favorable for different flexocoupling constants. The analytical predictions for the directions of the wave vectors are in agreement with the simulations. The analysis also provides good estimates for the critical values of the flexoelectric coefficients for the modulated phase formation as compared with our simulations. The analysis has also been applied to 2D modulated patterns, where it was shown that such patterns can be viewed as a superposition of two 1D modulations. Using the method of the degenerate perturbation theory we have studied the criteria for the formation of the 2D patterns. Such patterns are expected to arise in the case where the orientations of polarizations in the 1D modulated structures do not coincide with the favorable orientations of the spontaneous polarization in the homogeneous ferroelectric state.

Finally, we found that flexoelectric effects can strongly influence ferroelectric materials even in cases where no modulated phases appear. This underscores the need to carefully measure the flexoelectric coupling strenths in order to interpret recent experiments where flexoelectric effects have been shown to be important.

ACKNOWLEDGMENTS

This project was supported by the Swiss National Science Foundation and by a grant of the government of the Russian Federation 2012-220-03-434, Contract 14.B25.31.0025. The research leading to these results has also received funding from the European Research Council under the EU 7th Framework Program (FP7/2007-2013)/ERC Grant Agreement No. (268058) Mobile-W. Konstantin Shapovalov is acknowledged for numerical simulations of Eq. (35).

APPENDIX A: SIMULATIONS OF MECHNICALLY FREE SAMPLE USING PERIODIC BOUNDAY CONDITIONS

Here we expain the application to our problem of the method developed by Khachaturyan and co-workers [28] for simulations of mechanically free sample using periodic boundary conditions.

The electromechanical contribution to the free energy is expressed as

$$F_{\text{em}} = \int d\vec{r}\, f_{\text{em}}, \tag{A1}$$

where

$$\begin{aligned} f_{\text{em}} = {} & \frac{C_{11}}{2}\left[\left(u_{xx}-u_{xx}^0\right)^2+\left(u_{yy}-u_{yy}^0\right)^2\right]+C_{12}\left(u_{xx}-u_{xx}^0\right)\left(u_{yy}-u_{yy}^0\right)+\frac{C_{44}}{2}\left(u_{xy}-u_{xy}^0\right)^2 \\ & -\frac{f_{11}}{2}\left(P_x\frac{\partial u_{xx}}{\partial x}+P_y\frac{\partial u_{yy}}{\partial y}-u_{xx}\frac{\partial P_x}{\partial x}-u_{yy}\frac{\partial P_y}{\partial y}\right)-\frac{f_{12}}{2}\left(P_x\frac{\partial u_{yy}}{\partial x}+P_y\frac{\partial u_{xx}}{\partial y}-u_{xx}\frac{\partial P_y}{\partial y}-u_{yy}\frac{\partial P_x}{\partial x}\right) \\ & -\frac{f_{44}}{2}\left[P_x\frac{\partial u_{xy}}{\partial y}+P_y\frac{\partial u_{xy}}{\partial x}-u_{xy}\left(\frac{\partial P_y}{\partial x}+\frac{\partial P_x}{\partial y}\right)\right] \end{aligned} \tag{A2}$$

and u_{xx}^0, u_{yy}^0, and u_{xy}^0 are defined by Eq. (5) from the main text.

We decompose the strains into homogeneous and inhomogeneous parts as

$$u_{xx}=u_{xx}^h+\frac{\partial u_x}{\partial x}\,,\quad u_{yy}=u_{yy}^h+\frac{\partial u_y}{\partial y}\,,\quad u_{xy}=u_{xy}^h+\frac{\partial u_x}{\partial y}+\frac{\partial u_y}{\partial x}, \tag{A3}$$

where u_{ij}^h are the homogeneous (macroscopic) strains and u_i are the inhomogeneous displacements that are assumed to be periodic in the simulations. Substituting (A3) into (A2) into (A1) and retaining only terms involving u_{ij}^h we find

$$\begin{aligned} F_{\text{em}} = {} & \int d\vec{r}\,\frac{C_{11}}{2}\left[\left(u_{xx}^h\right)^2+\left(u_{yy}^h\right)^2-2u_{xx}^h\left(u_{xx}^0+\frac{\partial u_x}{\partial x}\right)-2u_{yy}^h\left(u_{yy}^0+\frac{\partial u_y}{\partial y}\right)\right] \\ & +\int d\vec{r}\,C_{12}\left[u_{xx}^h u_{yy}^h+u_{xx}^h\left(\frac{\partial u_y}{\partial y}-u_{yy}^0\right)+u_{yy}^h\left(\frac{\partial u_x}{\partial x}-u_{xx}^0\right)\right]+\int d\vec{r}\,\frac{C_{44}}{2}\left[\left(u_{xy}^h\right)^2-2u_{xy}^h\left(u_{xy}^0+\frac{\partial u_x}{\partial y}+\frac{\partial u_y}{\partial x}\right)\right] \\ & -\int d\vec{r}\left[\frac{f_{11}}{2}\left(u_{xx}^h\frac{\partial P_x}{\partial x}+u_{yy}^h\frac{\partial P_y}{\partial y}\right)+\frac{f_{12}}{2}\left(u_{xx}^h\frac{\partial P_y}{\partial y}+u_{yy}^h\frac{\partial P_x}{\partial x}\right)+\frac{f_{44}}{2}u_{xy}^h\left(\frac{\partial P_y}{\partial x}+\frac{\partial P_x}{\partial y}\right)\right]. \end{aligned} \tag{A4}$$

Since the polarizations and displacements are periodic, we can write

$$\int d\vec{r}\,\frac{\partial u_i}{\partial x_j}=0,\qquad \int d\vec{r}\,\frac{\partial P_i}{\partial x_j}=0\,, \tag{A5}$$

which leads to

$$\begin{aligned} F_{\text{em}} = {} & \frac{C_{11}}{2}\left\{\left[\left(u_{xx}^h\right)^2+\left(u_{yy}^h\right)^2\right]V-2u_{xx}^h\left(\int d\vec{r}\,u_{xx}^0\right)-2u_{yy}^h\left(\int d\vec{r}\,u_{yy}^0\right)\right\} \\ & +C_{12}\left[u_{xx}^h u_{yy}^h V-u_{xx}^h\left(\int d\vec{r}\,u_{yy}^0\right)-u_{yy}^h\left(\int d\vec{r}\,u_{xx}^0\right)\right]+\frac{C_{44}}{2}\left[\left(u_{xy}^h\right)^2 V-2u_{xy}^h\left(\int d\vec{r}\,u_{xy}^0\right)\right]. \end{aligned} \tag{A6}$$

The homogeneous stress components are calculated as

$$\begin{aligned} \sigma_{xx}^h &= \frac{1}{V}\frac{\partial F_{\text{em}}}{\partial u_{xx}^h}=C_{11}\left(u_{xx}^h-\frac{\int d\vec{r}\,u_{xx}^0}{V}\right)+C_{12}\left(u_{yy}^h-\frac{\int d\vec{r}\,u_{yy}^0}{V}\right), \\ \sigma_{yy}^h &= \frac{1}{V}\frac{\partial F_{\text{em}}}{\partial u_{yy}^h}=C_{11}\left(u_{yy}^h-\frac{\int d\vec{r}\,u_{yy}^0}{V}\right)+C_{12}\left(u_{xx}^h-\frac{\int d\vec{r}\,u_{xx}^0}{V}\right),\quad \sigma_{xy}^h=\frac{1}{V}\frac{\partial F_{\text{em}}}{\partial u_{xy}^h}=C_{44}\left(u_{xy}^h-\frac{\int d\vec{r}\,u_{xy}^0}{V}\right), \end{aligned} \tag{A7}$$

which may be expressed in terms of the average stress free strains as

$$\sigma^h_{xx} = C_{11}\big(u^h_{xx} - \langle u^0_{xx}\rangle\big) + C_{12}\big(u^h_{yy} - \langle u^0_{yy}\rangle\big), \quad \sigma^h_{yy} = C_{11}\big(u^h_{yy} - \langle u^0_{yy}\rangle\big) + C_{12}\big(u^h_{xx} - \langle u^0_{xx}\rangle\big),$$
$$\sigma^h_{xy} = C_{44}\big(u^h_{xy} - \langle u^0_{xy}\rangle\big). \tag{A8}$$

Clearly a system with $u^h_{ij} = \langle u^0_{ij}\rangle$ will correspond to a macroscopically stress free system, whereas $u^h_{ij} = 0$ describes a clamped system. Thus, to simulate a stress free system, the strains can be presented as follows:

$$u_{xx} = \langle u^0_{xx}\rangle + \frac{\partial u_x}{\partial x}, \quad u_{xx} = \langle u^0_{yy}\rangle + \frac{\partial u_y}{\partial y}, \quad u_{xy} = \langle u^0_{xy}\rangle + \frac{\partial u_x}{\partial y} + \frac{\partial u_y}{\partial x}. \tag{A9}$$

Using (A9), the equations of motion for the polarizations are expressed as

$$\begin{aligned}
-\frac{1}{\Gamma}\frac{\partial P_x}{\partial t} &= 2\alpha_1 P_x + 4\alpha_{11}P_x^3 + 2\alpha_{12}P_xP_y^2 + 6\alpha_{111}P_x^5 + \alpha_{112}\big(4P_x^3P_y^2 + 2P_xP_y^4\big)\\
&\quad - 2P_xQ_{11}\left[C_{11}\left(\langle u^0_{xx}\rangle + \frac{\partial u_x}{\partial x} - u^0_{xx}\right) + C_{12}\left(\langle u^0_{yy}\rangle + \frac{\partial u_y}{\partial y} - u^0_{yy}\right)\right]\\
&\quad - 2P_xQ_{12}\left[C_{11}\left(\langle u^0_{yy}\rangle + \frac{\partial u_y}{\partial y} - u^0_{yy}\right) + C_{12}\left(\langle u^0_{xx}\rangle + \frac{\partial u_x}{\partial x} - u^0_{xx}\right)\right] - Q_{44}P_y\left[C_{44}\left(\langle u^0_{xy}\rangle + \frac{\partial u_x}{\partial y} + \frac{\partial u_y}{\partial x} - u^0_{xy}\right)\right]\\
&\quad - f_{11}\left(\frac{\partial^2 u_x}{\partial^2 x}\right) - f_{12}\left(\frac{\partial^2 u_y}{\partial x\partial y}\right) - f_{44}\left(\frac{\partial^2 u_x}{\partial^2 y} + \frac{\partial^2 u_y}{\partial y\partial x}\right) - \lambda_1\nabla^2 P_x + \lambda_2\nabla^2(\nabla^2 P_x) + \frac{\partial\varphi}{\partial x},\\
-\frac{1}{\Gamma}\frac{\partial P_y}{\partial t} &= 2\alpha_1 P_y + 4\alpha_{11}P_y^3 + 2\alpha_{12}P_yP_x^2 + 6\alpha_{111}P_y^5 + \alpha_{112}\big(4P_y^3P_x^2 + 2P_yP_x^4\big)\\
&\quad - 2P_yQ_{11}\left[C_{11}\left(\langle u^0_{yy}\rangle + \frac{\partial u_y}{\partial y} - u^0_{yy}\right) + C_{12}\left(\langle u^0_{xx}\rangle + \frac{\partial u_x}{\partial x} - u^0_{xx}\right)\right]\\
&\quad - 2P_yQ_{12}\left[C_{11}\left(\langle u^0_{xx}\rangle + \frac{\partial u_x}{\partial x} - u^0_{xx}\right) + C_{12}\left(\langle u^0_{yy}\rangle + \frac{\partial u_y}{\partial y} - u^0_{yy}\right)\right] - Q_{44}P_x\left[C_{44}\left(\langle u^0_{xy}\rangle + \frac{\partial u_x}{\partial y} + \frac{\partial u_y}{\partial x} - u^0_{xy}\right)\right]\\
&\quad - f_{11}\left(\frac{\partial^2 u_y}{\partial^2 y}\right) - f_{12}\left(\frac{\partial^2 u_x}{\partial x\partial y}\right) - f_{44}\left(\frac{\partial^2 u_y}{\partial^2 x} + \frac{\partial^2 u_y}{\partial x\partial y}\right) - \lambda_1\nabla^2 P_y + \lambda_2\nabla^2(\nabla^2 P_y) + \frac{\partial\varphi}{\partial y}.
\end{aligned} \tag{A10}$$

The dynamics of the inhomogeneous displacements are given by the dissipative force balance equations

$$\rho\frac{\partial^2 u_x}{\partial t^2} - \eta\nabla^2\frac{\partial u_x}{\partial t} = \frac{\partial\sigma_{xx}}{\partial x} + \frac{\partial\sigma_{xy}}{\partial y}, \quad \rho\frac{\partial^2 u_y}{\partial t^2} - \eta\nabla^2\frac{\partial u_y}{\partial t} = \frac{\partial\sigma_{xy}}{\partial x} + \frac{\partial\sigma_{yy}}{\partial y}, \tag{A11}$$

where the stresses are calculated as

$$\begin{aligned}
\sigma_{xx} &= C_{11}\left(\langle u^0_{xx}\rangle + \frac{\partial u_x}{\partial x} - u^0_{xx}\right) + C_{12}\left(\langle u^0_{yy}\rangle + \frac{\partial u_y}{\partial y} - u^0_{yy}\right) + \left[f_{11}\left(\frac{\partial P_x}{\partial x}\right) + f_{12}\left(\frac{\partial P_y}{\partial y}\right)\right],\\
\sigma_{yy} &= C_{11}\left(\langle u^0_{yy}\rangle + \frac{\partial u_y}{\partial y} - u^0_{yy}\right) + C_{12}\left(\langle u^0_{xx}\rangle + \frac{\partial u_x}{\partial x} - u^0_{xx}\right) + \left[f_{11}\left(\frac{\partial P_y}{\partial y}\right) + f_{12}\left(\frac{\partial P_x}{\partial x}\right)\right],\\
\sigma_{xy} &= C_{44}\left(\langle u^0_{xy}\rangle + \frac{\partial u_x}{\partial y} + \frac{\partial u_y}{\partial x} - u^0_{xy}\right) + f_{44}\left[\left(\frac{\partial P_y}{\partial x}\right) + \left(\frac{\partial P_x}{\partial y}\right)\right],
\end{aligned} \tag{A12}$$

Equations (5), (A10), (A11), and (A12) are solved using finite difference methods, assuming periodic boundary conditions for displacements and polarizations. This will ensure a macroscopically stress-free system. This can also be inferred by performing spatial average of the stresses in (A12). Using conditions (A5), it can be seen that $\langle\sigma_{ij}\rangle = 0$.

APPENDIX B: DERIVATION OF CRITICAL WAVE VECTORS

Here we derive the directions and magnitudes of possible wave vectors of the modulated phase by solving the eigenvalue problem in Eq. (17).

The modulated phase occurs when the smallest eigenvalue ω_- in (17) becomes negative. The function $\omega_-(\vec{k})$ can be defined as the smallest root of the characteristic polynomial for the matrix M_{ij} in (17),

$$A_0(\vec{k}) + A_1(\vec{k})\omega_- + A_2(\vec{k})\omega_-^2 + \cdots = 0, \tag{B1}$$

where $A_0 = \det[M], A_1, A_2, \ldots$ are determined from the matrix M_{ij} in (17). Note that Eq. (B1) holds for all $\vec{k}$. Differentiation of (B1) with respect to the components of the

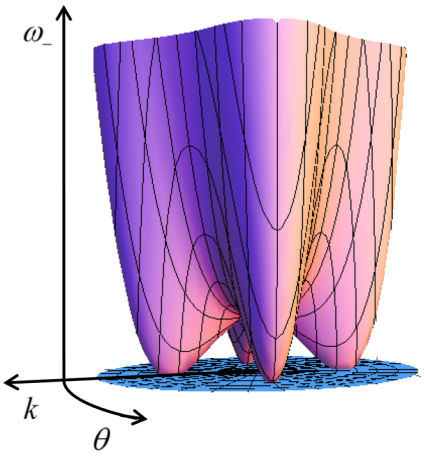

FIG. 9. (Color online) Schematics of the dependence of ω_- on the magnitude of the wave vector k and its direction θ for the case where the minima are in the $\langle 01 \rangle$ direction.

wave vector yields

$$\frac{\partial A_0}{\partial \vec{k}} + A_1 \frac{\partial \omega_-}{\partial \vec{k}} + \frac{\partial A_1}{\partial \vec{k}} \omega_- + 2A_2 \omega_- \frac{\partial \omega_-}{\partial \vec{k}} + \frac{\partial A_2}{\partial \vec{k}} \omega_-^2 + \cdots = 0, \tag{B2}$$

where we introduced the differential operator

$$\frac{\partial}{\partial \vec{k}} = \left\{ \frac{\partial}{\partial k_x}, \frac{\partial}{\partial k_y} \right\}$$

The behavior of the function $\omega_-(\vec{k})$ is schematically plotted in Fig. 9.

The critical vector $\vec{k}_{\min} \neq 0$ is defined by

$$\omega_-(\vec{k}_{\min}) = 0, \quad \frac{\partial \omega_-}{\partial \vec{k}} \bigg| \vec{k} = \vec{k}_{\min} = 0, \tag{B3}$$

In view of Eq. (B3), at the point $\vec{k} = \vec{k}_{\min}$, Eq. (B2) is reduced to $\partial A_0 / \partial \vec{k} = 0$. Thus, using Eqs. (B1)–(B3) the conditions for the critical wave vectors may be formulated in terms of determinant of the matrix $\hat{M}$ governing the eigenvalue problem:

$$\det[\hat{M}] = 0, \quad \frac{\partial}{\partial \vec{k}} \det[\hat{M}] = 0. \tag{B4}$$

Rather than simply applying condition (B4) to the matrix $[4 \times 4]$ in (16) it is preferable to make simplifications to the matrix. Specifically, the rank of the matrix can be decreased from 4 to 3 if one uses the reference frame related to the wave vector. In view of the high electrostatic energy associated with longitudinal polarization gradients, the lowest eigenvalues of (16) will correspond to transverse modes, in which $\vec{k} \cdot \vec{P} = 0$. This condition is automaticaly taken into account by making a coordinate transform into the reference frame where the wave vector $\vec{k}$ and the polarization $\vec{P}$ are directed along axes x_1 and x_2, respectively. In the $x_1 x_2$ reference frame, the stability problem has the form

$$\begin{pmatrix} \mathrm{M}_{11} & \mathrm{M}_{12} & \mathrm{M}_{13} \\ \mathrm{M}_{12} & \mathrm{M}_{22} & \mathrm{M}_{23} \\ \mathrm{M}_{13} & \mathrm{M}_{23} & \mathrm{M}_{33} \end{pmatrix} \begin{pmatrix} P_2 \\ u_1 \\ u_2 \end{pmatrix} = \omega \begin{pmatrix} P_2 \\ u_1 \\ u_2 \end{pmatrix}, \tag{B5}$$

where

$$M_{11} = \alpha + k^2 \lambda_1 + k^4 \lambda_2, \quad M_{12} = \tfrac{1}{2} k^2 \sin(4\theta)(f_{11} - f_{12} - 2f_{44}),$$
$$M_{13} = k^2 [\sin^2(2\theta) f_{11} - \sin^2(2\theta) f_{12} + 2\cos^2(2\theta) f_{44}], \quad M_{22} = \tfrac{1}{4} k^2 \{[3 + \cos(4\theta)] C_{11} + 2\sin^2(2\theta)(C_{12} + 2C_{44})\},$$
$$M_{23} = \tfrac{1}{2} k^2 \sin(4\theta)(C_{11} - C_{12} - 2C_{44}), \quad M_{33} = -\tfrac{1}{4} k^2 \{[-1 + \cos(4\theta)] C_{11} + 2\sin^2(2\theta) C_{12} - 4\cos^2(2\theta) C_{44}\}. \tag{B6}$$

Here $k = |\vec{k}|$, θ is the angle between $\vec{k}$ and the crystallographic x axis. In polar coordinates, the condition (B4) may be written in the form

$$\det[\hat{M}] = 0, \quad \frac{\partial}{\partial k} \det[\hat{M}] = 0, \quad \frac{\partial}{\partial \theta} \det[\hat{M}] = 0. \tag{B7}$$

For the matrix M_{ij} with components defined by (B6), conditions (B7) are satisfied only in two cases:

$$\theta = \frac{\pi N}{2}, \quad N = 0,1,2,3, \quad k_{\min} = \frac{\sqrt{-\lambda_1 c_{44} + f_{44}^2}}{\sqrt{2}\sqrt{\lambda_2}\sqrt{c_{44}}}, \quad \alpha = \frac{\left(\lambda_1 c_{44} - f_{44}^2\right)^2}{4\lambda_2 c_{44}^2}, \tag{B8}$$

and

$$\theta = \frac{\pi}{4} + \frac{\pi N}{2}, \quad N = 0,1,2,3, \quad k_{\min} = \frac{\sqrt{C_{11} + C_{12} + 2C_{44}} \sqrt{2\lambda_1 C_{11} - 2\lambda_1 C_{12} - f_{11}^2 + 2f_{11} f_{12} - f_{12}^2}}{\sqrt{-4\lambda_2 C_{11}^2 + 4\lambda_2 C_{12}^2 - 8\lambda_2 C_{11} C_{44} + 8\lambda_2 C_{12} C_{44}}},$$
$$\alpha = \frac{\left(2\lambda_1 C_{11} - 2\lambda_1 C_{12} - f_{11}^2 + 2f_{11} f_{12} - f_{12}^2\right)^2}{16\lambda_2 (C_{11} - C_{12})^2}. \tag{B9}$$

Thus, function $\omega_-(\theta, k)$ has minima corresponding to the high symmetry directions $\theta = \pi N/2$ [Eq. (B8)] or $\theta = \frac{\pi}{4} + \pi N/2$ [Eq. (B9)], where $N = 0,1,2,3$. We derive expressions for the values of $\omega_-(k)$ in these two cases by substituting $\theta = 0$ or $\theta = \frac{\pi}{4}$ into Eqs. (B6).

For the ⟨01⟩ orientation we obtain

$$\hat{M}^{\langle 01\rangle} = \begin{pmatrix} (\alpha + k^2\lambda_1 + k^4\lambda_2) & 0 & k^2 f_{44} \\ 0 & k^2 C_{11} & 0 \\ k^2 f_{44} & 0 & k^2 C_{44} \end{pmatrix}, \tag{B10}$$

from which we find

$$\omega_-(01) = \alpha + k^2\left(\lambda_1 - \frac{f_{44}^2}{C_{44}}\right) + k^4\lambda_2. \tag{B11}$$

For the ⟨11⟩ orientation we obtain

$$\hat{M}^{\langle 11\rangle} = \begin{pmatrix} (\alpha + k^2\lambda_1 + k^4\lambda_2) & 0 & \frac{1}{2}k^2(f_{11} - f_{12}) \\ 0 & \frac{1}{2}k^2[C_{11} + (C_{12} + 2C_{44})] & 0 \\ \frac{1}{2}k^2(f_{11} - f_{12}) & 0 & \frac{1}{2}k^2(C_{11} - C_{12}) \end{pmatrix}, \tag{B12}$$

from which we find

$$\omega_-(11) = \alpha + k^2\left[\lambda_1 - \frac{(f_{11} - f_{12})^2}{2(C_{11} - C_{12})}\right] + k^4\lambda_2. \tag{B13}$$

The dependence of ω_- on the magnitude of k and the direction θ of the wave vector is schematically shown in Fig. 9.

[1] A. K. Tagantsev, L. E. Cross, and J. Fousek, *Domains in Ferroic Crystals and Thin Films*, 1st ed. (Springer, Berlin, 2010).

[2] P. V. Yudin, A. K. Tagantsev, E. A. Eliseev, A. N. Morozovska, and N. Setter, Phys. Rev. B **86**, 134102 (2012).

[3] E. A. Eliseev, A. N. Morozovska, G. S. Svechnikov, P. Maksymovych, and S. V. Kalinin, Phys. Rev. B **85**, 045312 (2012).

[4] V. L. Indenbom, E. B. Loginov, and M. A. Osipov, Kristalografija **26**, 1957 (1981).

[5] Sh. M. Kogan, Sov. Phys. Solid State **5**, 2069 (1963).

[6] P. Zubko, G. Catalan, A. Buckley, P. R. L. Welche, and J. F. Scott, Phys. Rev. Lett. **99**, 167601 (2007).

[7] M. S. Majdoub, P. Sharma, and T. Cagin, Phys. Rev. B **77**, 125424 (2008).

[8] W. Zhu, J. Y. Fu, N. Li, and L. E. Cross, Appl. Phys. Lett. **89**, 192904 (2006).

[9] A. Gruverman, B. J. Rodriguez, A. I. Kingon, R. J. Nemanich, A. K. Tagantsev, J. S. Cross, and M. Tsukuda, Appl. Phys. Lett. **83**, 728 (2003).

[10] H. Lu, C.-W. Bark, D. Esque. De los Ojos, J. Alcala, C. B. Eom, G. Catalan, and A. Gruverman, Science **336**, 59 (2012).

[11] D. Lee, A. Yoon, S. Y. Jang, J.-G. Yoon, J.-S. Chung, M. Kim, J. F. Scott, and T. W. Noh, Phys. Rev. Lett. **107**, 057602 (2011).

[12] G. Catalan, A. Lubk, A. H. G. Vlooswijk, E. Snoeck, C. Magen, A. Janssens, G. Risspens, G. Rijnders, D. H. A. Blank, and B. Noheda, Nat. Mater. **10**, 966 (2011).

[13] E. A. Eliseev, A. N. Morozovska, M. D. Glinchuk, and R. Blinc, Phys. Rev. B **79**, 165433 (2009).

[14] S. Hiboux, P. Muralt, and T. Maeder, J. Mater. Res. **14**, 4307 (1999).

[15] S. Wada, K. Yako, H. Kakemoto, T. Tsurumi, and T. Kiguchi, J. Appl. Phys. **98**, 014109 (2005).

[16] M. Davis, D. Damjanovic, D. Hayem, and N. Setter, J. Appl. Phys. **98**, 014102 (2005).

[17] A. D. Bruce and R. A. Cowley, *Structural Phase Transitions* (Taylor and Francis, London, 1981).

[18] J. D. Axe, J. Harada, and G. Shirane, Phys. Rev. B **1**, 1227 (1970).

[19] R. Blinc and A. P. Levanyuk, in *Modern Problems in Condensed Matter*, edited by V. M. Agranovich and A. A. Maradudin (North Holland, Amsterdam, 1986), p. 410.

[20] J. Petzelt, Phase Trans. **2**, 155 (1981).

[21] I. Maclaren, R. Villaurrutia, and A. Pelaiz-Barranco, J. Appl. Phys. **108**, 034109 (2010).

[22] T. A. Aslanian and A. P. Levanyuk, Solid State Commun. **31**, 547 (1979).

[23] R. Oshima, M. Sugiyama, and F. E. Fujita, Metal. Trans. A **19**, 803 (1988).

[24] K. Dayal and K. Bhattacharya, Acta Mater. **55**, 1907 (2007).

[25] A. K. Tagantsev, Ferroelectrics **375**, 19 (2008).

[26] J. Hlinka and P. Marton, Phys. Rev. B **74**, 104104 (2006).

[27] B. Houchmanzadeh, J. Lajzerowicz, and E. Salje, Phase Trans. **38**, 77 (1992).

[28] A. Artemev, Y. Jin, and A. G. Khachaturyan, Acta Materialia **49**, 1165 (2001).

[29] M. J. Haun, Z. Q. Zhuang, E. Furman, S. J. Jang, and L. E. Cross, Ferroelectrics **99**, 45 (1989).

[30] W. J. Merz, Phys. Rev. **95**, 690 (1954).

[31] I. Naumov, L. Bellaiche, and H. Fu, Nature (London) **432**, 737 (2004).

[32] N. Ng, R. Ahluwalia, and D. J. Srolovitz, Acta Mater. **60**, 3632 (2012).

[33] L. W. Chang, V. Nagarajan, J. F. Scott, and J. M. Gregg, Nano Lett. **13**, 2553 (2013).